Nature Communications

https://doi.org/10.1038/s41467-026-73474-6

Article in Press

Dual platform spatial transcriptomics reveals parvalbumin interneuron subtype vulnerability in mouse models of Alzheimer's disease

Received: 13 March 2025

Accepted: 13 May 2026

Cite this article as: Seo, H., Terstege, D.J., Ren, Y. *et al.* Dual platform spatial transcriptomics reveals parvalbumin interneuron subtype vulnerability in mouse models of Alzheimer's disease. *Nat Commun* (2026). https://doi.org/10.1038/s41467-026-73474-6

Heewon Seo, Dylan J. Terstege, Yi Ren, Shiying Liu, Kimberly-Ann Ruth Goring, Bo Young Ahn & Jonathan R. Epp

Dual platform spatial transcriptomics reveals parvalbumin interneuron subtype vulnerability in mouse models of Alzheimer's disease

Heewon Seo[1], Dylan J. Terstege[2,3], Yi Ren[2,3], Shiying Liu[1], Kimberly-Ann Ruth Goring[1], Bo Young Ahn[1], Jonathan R. Epp[2,3*]

[1] Applied Spatial Omics Centre, Cumming School of Medicine, University of Calgary, Calgary, AB, Canada
[2] Department of Cell Biology and Anatomy, Cumming School of Medicine, University of Calgary, Calgary, AB, Canada
[3] Hotchkiss Brain Institute, University of Calgary, Calgary, AB, Canada

*To whom correspondence should be addressed. Email: Jonathan.Epp1@ucalgary.ca

Abstract

Alzheimer's disease (AD) is a progressive neurodegenerative disorder characterized by cognitive decline and synaptic dysfunction. Among the earliest regions affected is the retrosplenial cortex (RSC), where parvalbumin-expressing (PV+) interneurons are particularly susceptible to AD-related pathology. To understand the molecular alterations within these vulnerable neurons we employed a dual-platform spatial transcriptomics approach, **integrating GeoMx Digital Spatial Profiler (DSP) and Xenium In Situ. We analyzed the transcriptomic profiles of PV+ and NeuN+ neurons in the RSC of female 5xFAD mice.** We leveraged the individual strengths of each platform to generate a robust and comprehensive dataset. Using non-negative matrix factorization and k-means clustering, we identified disease-associated metagenes and examined their spatial distribution. Our analysis revealed distinct transcriptional subpopulations within PV+ interneurons, with specific metagenes differentially expressed in RSC. ***Dner*, *Gad1*, and *Pvalb* exhibited significant down-regulation in TG mice, suggesting impairments in PV+ interneuron function and GABAergic signalling.** Cross-validation between GeoMx DSP and Xenium In Situ as well as RNAscope and immunohistochemistry confirmed the reproducibility and robustness of these findings. This study provides insights into the heterogeneity and molecular vulnerabilities of PV+ interneurons in AD and demonstrates the power of integrating spatial transcriptomic platforms to uncover disease-associated neuronal subtypes and molecular markers.

Introduction

Alzheimer's disease (AD) is characterized by progressive cognitive decline and the pathological accumulation of amyloid plaques and neurofibrillary tau tangles. Additionally, AD has also been associated with impairments in brain glucose metabolism, with this change often arising even prior to the onset of cognitive decline[1,2]. Impaired metabolic activity is particularly interesting within the context of AD pathogenesis as while it may impact large brain regions, different cell types will be variably vulnerable or resilient to metabolic stress; therefore, yielding the potential of identifying cell-type specific vulnerabilities in AD[3]. The retrosplenial cortex (RSC) is among the first regions in which hypometabolic activity can be observed during AD pathogenesis[4,5]. These metabolic impairments in the RSC seem to be particularly influential on the parvalbumin-expression neuron populations (PV+)[6,7]. These cells are the primary source of GABAergic inhibition within this region and require considerable metabolic resources to maintain their high basal firing rate[8]. Without adequate energetic resources, these cells are unable to regulate the activity of their networks of pyramidal neurons, which can have drastic consequences on functional connectivity and cognitive function[9,10]. Therefore, the study of PV+ populations within this region during early AD pathogenesis is of particular interest as it can lead to the identification of factors which can modulate the vulnerability of these neurons to the metabolic pressures of AD and, ultimately, aid in combating cognitive decline.

While there have been functional assessments of the PV+ neuron populations in the RSC[11,12], the uniformity of their spatial transcriptomic fingerprints is unknown in AD. Some data has suggested that the functional impairments observed in these cells are heterogeneous, with seemingly not all PV+ cells showing impairments during early AD pathogenesis[12,13]; however, this has never been formally shown on a transcriptional level. Part of the issue with this has been methodological, wherein unbiased single-cell spatial transcriptomic techniques, such as the Xenium In Situ from 10X Genomics, require cell type inferences based on expression profile libraries. In disease, it is expected that these transcriptional profiles may no longer align with libraries generated under physiological conditions[14–16]. While not a single-cell platform, the GeoMx Digital Spatial Profiler (DSP) from Nanostring allows users to stain for proteins of interest and perform bulk RNA-seq on the nuclei within these stained cellular areas[17]. Unbiased *k*-means clustering applied to bulk RNA-seq data from a GeoMx DSP dataset identifies subpopulations of PV+ neurons in the RSC in AD. These fingerprints of these subpopulations can then be applied to Xenium In Situ single-cell datasets to further parse the identity of disease-associated profiles of the spatially resolved nuclei in these datasets.

In the current study, we aimed to identify distinct transcriptional signatures that may represent biologically meaningful subpopulations to better understand the molecular heterogeneity of PV+ and NeuN+ neuronal populations in the RSC during AD progression. Our analysis specifically sought to reveal neuronal subtypes that exhibit differential vulnerability to AD pathology by identifying gene expression patterns enriched in either transgenic (TG) or wild-type (WT) mice. Therefore, we leveraged the cell-type specificity of GeoMx DSP and the single-cell resolution of Xenium In Situ to examine the spatial transcriptomic profile of PV+ and PV− neurons across the RSC in a mouse model of AD. In doing so, we characterized the heterogeneity in the transcriptomic profiles of PV+ interneuron populations across the RSC. With these profiles, we identified distinct disease-associated molecular markers within PV+ populations. From these disease-associated gene clusters, we identified impaired expression of critical genes across many metabolic, electrophysiological, GABAergic, and synaptic processes – corresponding with many of the previously described impairments observed in RSC PV+ interneuron populations in 5xFAD mice. By identifying transcriptional changes specific to PV+ interneurons using spatial transcriptomics, this study provides insight into specific mechanisms that may underlie differential vulnerability across PV+ interneuron populations during the critical, early, stages of AD pathogenesis. In doing so, we identify transcriptomic markers of particularly vulnerable neuron populations, which can assist in the development of future therapeutic targets. Furthermore, this combination of spatial transcriptomic analyses allowed for integration of these two datasets. Using GeoMx transcriptomic data collected from PV+ and PV− neuron populations of the RSC, we identified disease-associated metagene clusters which were specific to PV+ sub-populations. These metagene clusters were then used as cell-type references for single-cell Xenium In Situ, where it was identified that the proportion and distribution of disease-associated factors change in AD. Biologically, these results highlight that PV+ populations are not homogenous across the RSC in AD and identify particular risk factors which are associated with AD. Methodologically, we demonstrate the high degree of between-method coherence for the GeoMx DSP and Xenium In Situ spatial transcriptomic platforms and provide the framework and methodologies for their combined integration in future studies.

Results

Image-based spatial transcriptomics enables cell-type-specific profiling

In our study, **we employed Nanostring GeoMx DSP to explore the molecular characteristics of interneurons within the RSC** (Fig. 1a). The experiment included brain hemisections from four 5xFAD

TG female mice and three WT female mice. These samples were arranged on a single slide for GeoMx DSP experiments (Fig. 1b). Additionally, consecutive sections from six samples (three TGs and three WTs) were similarly prepared on another slide for validation. Our methodological approach utilized morphology-based segmentation to determine four distinct transcriptome segments: (1) **PV interneurons** and **neurons**, identified by their expressions of PV and NeuN, respectively; (2) **Amyloid-positive cells**, isolated through Amyloid expression; and (3) Cells devoid of PV, NeuN, and Amyloid expression (triple-negative [TN]), which includes endothelial cells, fibroblasts, and similar cell types (Fig. 1c). The dataset generated from this study encompasses 20,175 probes within the Whole-transcriptomics Atlas (WTA) panel. Subsequently, we pinpointed 14 regions of interest (ROIs) in the RSC, assigning two ROIs per sample to refine our analysis further. All four segments were profiled whenever feasible, yielding 46 AOIs (area-of-illuminations)—14 PVs, 14 NeuNs, four Amyloids, and 14 TNs. No Amyloid segment was captured from WT samples. To ensure the integrity of our findings, we implemented quality assessment protocols using the R package *GeomxTools* developed by Nanostring and the R package *DESeq2* for normalizing the raw count matrix (Fig. 1d and see Methods). Our analysis revealed a positive correlation between the number of nuclei and the area size (μm^2) with the TN segment exhibiting a more extensive area size compared to others (Fig. 1e). However, we observed that larger AOIs tend to have a higher background signal, or limit of quantification (LOQ), leading to the exclusion of many genes (Fig. 1f). Despite the Amyloid and NeuN segments having comparable LOQ values, a more significant number of genes were excluded in the Amyloid segment due to a lower nucleus count. None of the AOIs covered more than 10% of the genes in either the TN or Amyloid segments, and one PV AOI was excluded due to insufficient coverage (Fig. 1g). Following normalization, a principal component analysis (PCA) was conducted to examine the data properties. The PCA results highlighted a significant difference between the PV and NeuN with their respective AOIs clustering at opposite ends (Fig. 1h). This distinction underscores the unique molecular profiles inherent to each segment, and it emphasizes the potential for further research into the molecular dynamics of the RSC.

Identification of the Interneuron- and Neuron-specific genes

Following the QC steps, **7,262 genes underwent normalization and downstream analysis in 26 AOIs**. No significant differences were observed between WT and TG mice in the number of nuclei per mouse within each PV and NeuN segment (Supplementary Table S1). Initially, we identified interneuron- and neuron-specific genes by comparing the PV (N=6) and NeuN (N=6) segments in WT

mice. The differential expression analysis was conducted under stringent criteria, establishing a false discovery rate (FDR) threshold of less than 0.05 and an absolute log2 fold change (Log2FC) exceeding 0.2 (see Methods). We found 60 up-regulated and 27 down-regulated genes in PV (Fig. 1i). Notably, *Erbb4*, a key NRG1 receptor, showed statistical significance (Log2FC=0.615, *P*-value=0.0002, FDR=0.0301), consistent with previous reports[18], that has an association with schizophrenia[19] and AD[20]. Additionally, *Pvalb* (parvalbumin; Log2FC=0.373, *P*-value=0.0003, FDR=0.0342) and *Btbd11* (Log2FC=0.398, *P*-value=2.8E-05, FDR=0.0179) were identified as interneuron-specific markers with relevance to neurological diseases[21] or brain function[22]. On the other hand, *Cadps2* (Log2FC=−0.300, *P*-value=2.0E-06, FDR=0.0086) encodes a member of the calcium-dependent activator of secretion protein in neurons, and *Adcy2* (Log2FC=−0.364, *P*-value=0.0003, FDR=0.0332) is a membrane-associated enzyme predominantly expressed in neurons.

Deconvolution and correlation networks revealed meaningful biological modules

Non-negative matrix factorization (NMF) was employed to deconvolve analysis-ready profiles across distinct segments, enabling the extraction of latent gene expression patterns. Metagenes are defined as the basis (the *W* matrix) components obtained from NMF[23], each representing a weighted combination of genes that tend to co-express across the dataset. These metagenes capture underlying biological signals and can reflect coordinated pathways, cell types, or functional programs. Specifically, each metagene is a vector of non-negative weights, indicating the contribution of each gene to that latent factor. In our implementation of NMF, we established the minimum and maximum ranks at two and ten, respectively. However, we included ranks [2, **6**] and [2, **7**] from the NMF results corresponding to PV and NeuN segments, respectively, for the subsequent analysis. This approach allowed us to exclude higher ranks which elucidate the finer resolution of metagenes[24], including those that are sample-specific or biologically less meaningful. We selected a rank range that allowed us to capture meaningful biological diversity without overfitting to sample-specific noise. The chosen ranks maximized the recovery of stable, interpretable metagenes while preserving distinct communities that were differentially represented in TG and WT mice. Consequently, the maximum ranks were set at half of the sample sizes within each segment (Fig. 2a). In the PV segment, we concatenated 20 (2+3+4+5+6) *W* matrices and calculated correlation coefficients column-wide. Among the 190 (20×19÷2) possible pairs, 30 pairs of the 20 metagenes demonstrated a positive correlation (Spearman rho >0.5). This led to the generation of a correlation network, wherein nodes represent metagenes, and links (edges) are established between metagenes when Spearman rho >0.5. Utilizing the community detection algorithm,

four distinct communities were identified within the network comprising three larger communities and a singular two-node community. While heuristics often serve as a consensus method for selecting the optimal rank from NMF results, our approach was data-driven. Specifically, three metagenes (*k*=1, 2, and 3) at rank=3 were identified as members across all communities except the two-node community (Community *#4*). This methodology entailed labelling metagenes at each rank within the correlation network and evaluating the inclusion of communities at given ranks for downstream analysis under the assumption that each metagene could represent a distinct biological module or community. An increase to rank=4 resulted in the fourth metagene being redundantly labelled within Community *#3* (Supplementary Fig. S1). This redundancy suggests a similarity in biological features between the two metagenes, negating the need for profiling both. Consequently, **rank=3 was selected for downstream analysis of the PV segment**, and rank=4 for the NeuN segment. Interestingly, Community *#4*, at high ranks (*k*=1 at rank five and *k*=6 at rank six), was a minor component within the PV segment and was excluded from downstream analysis. Lastly, assigning a sample to each metagene at the chosen rank for each segment was conducted using the *H* matrix (see Methods). For instance, WT2F−PV−002 demonstrated the highest value in $M1^{PV}$ (metagene 1 in PV), whereas TG4F−PV−007 exhibited the highest value in $M2^{PV}$ (Supplementary Fig. S2). Within the PV segment, **$M1^{PV}$ and $M2^{PV}$ were exclusively linked to the WT and TG specimens, respectively, with $M3^{PV}$ representing a mixed category**.

Metagenes-specific features recapitulate 5xFAD model

In delineating the characteristics of each metagene, we employed a methodology that involved the extraction of metagene-associated genes (MAGs) by utilizing *W*/*H* matrices and expression profiles (see Methods). This analytical approach resulted in the identification of distinct sets of MAGs for each metagene category, specifically 97 MAGs for $M1^{PV}$, 94 MAGs for $M2^{PV}$, and 79 MAGs for $M3^{PV}$, with a notable absence of gene overlap between the MAGs of $M1^{PV}$ and $M2^{PV}$ (Fig. 2b and Supplementary Table S2). Further characterization of these MAGs was achieved through the execution of an enrichment test which leveraged the hypergeometric distribution in conjunction with well-established gene sets (see Methods). The findings from this test revealed a significant enrichment of $M1^{PV}$ MAGs in terms related to cellular components (CC), whereas $M2^{PV}$ MAGs exhibited enrichment in terms pertinent to biological processes (BP) (Fig. 2c and Supplementary Table S3). A particularly interesting finding was that **the negative regulation of neuron apoptotic process emerged as notably significant**

among the terms significantly associated with *M2*^{PV} MAGs. This term holds substantial relevance due to its significant association with neurodegenerative conditions, such as AD[25,26].

Biological modules showed mutual exclusivity between TG and WT

Each specimen exhibits distinct molecular characteristics and a heterogeneous composition of metagenes. Consequently, a correlation network was generated for each specimen, and nodes were annotated based on the highest coefficient value to elucidate the predominant community within each sample (Fig. 2d, Supplementary Fig. S3, and see Methods). Significantly, TG4F demonstrated a pronounced enrichment for Community *#2* and *#3*, with six out of eight and three out of four metagenes being pinpointed, respectively. On the other hand, Community *#1*, which is associated with WT, did not feature any metagenes. In contrast, WT2F is associated with all metagenes within Community *#1* while showing sparse representation in other communities. Additionally, a co-occurrence of diverse metagenes was observed in TG3F (Communities *#2* and *#3*) and WT1F (Communities *#1* and *#3*), indicating a complex interplay of genetic elements. Noticeably, the absence of MAGs intersection between *M1*^{PV} and *M2*^{PV} underscores the exclusive nature of the overrepresentation between Communities *#1* and *#2*. The relationship between metagenes and specimens was quantified using coefficient values (*H* matrix). However, reliance on maximal values alone may mislead the interpretation as a single specimen's profile cannot be sufficiently explained by a singular metagene or coefficient value. To address this, we incorporated a comprehensive approach by calculating the geometric mean of coefficient values for each specimen (Fig. 2e). A circular bar plot was employed to visually represent the geometric mean where a taller bar indicates a metagene's more significant contribution to the specimen's profile. Surprisingly, ***M1*^{PV} was minimally present across all TG specimens, yet it reported the lowest impact among PV metagenes. Meanwhile, the proportionality of *M2*^{PV} and *M3*^{PV} varied across TG specimens, suggesting inter-sample variability**. Besides, *M2*^{PV} exhibited a uniform presence across WT specimens, whereas *M3*^{PV} in WT1F and *M1*^{PV} in WT2F were identified as having the most substantial contributions.

Spatial transcriptomics at the single-cell level captured high-quality data

In this study, we employed the Xenium In Situ platform to gain spatially resolved insights into the molecular architecture of interneurons within the RSC, which enabled the capture of data from 247 distinct genes. This approach enabled high-resolution transcriptomic profiling of targeted neuronal populations in situ, facilitating a detailed characterization of their gene expression signatures within the complex brain tissue microenvironment. The quantification of tissue region areas across the samples

revealed a comparable range, extending from 21 million (M) to 28M square micrometres (μm^2), with an approximate detection of 50,000 cells per sample, culminating in a total of 303,158 cells (Fig. 3a). The introduction of Unassigned Transcriptomes (UTx) was observed, which can be attributed to the inherent tissue structure. The proportion of UTx varies by tissue type. In the context of the non-diseased mouse brain, it is typically reported that UTx comprises about 20-30% of the total, a range within which all our examined samples fall (26.3 ± 3.6% [mean and standard deviation]). Initially, under-segmented cells were identified using Grubb's test, leading to their exclusion for *P*-values <0.05. Despite the standardization of centroid diameter, i.e., nucleus size, per tissue type in the Xenium instrument, challenges in cell segmentation arise due to tissue slicing and three-dimensional structures, resulting in the detection of 28 outlier cells in terms of area size (see Methods). Each sample presented a minimum of two outliers, with a notable 11 outliers identified in TG2F. Cells exhibiting low Tx detected, indicative of low-quality cells, were excluded when ten or fewer Tx were identified within a cell. Statistical analysis revealed no significant difference between TG and WT groups (two-sided Wilcoxon rank-sum test, *P*-value=0.763), excluding 1,312 low-quality cells. The predesigned panel (*N*=247) lacks positive controls; the study leveraged negative controls to exclude cells demonstrating significant background signals. Cells were filtered out when the proportion of the number of negative probes detected out of all probes identified exceeded 5%, underpinning the premise that such signals were unlikely to be genuine, resulting in 221 cells being filtered out due to elevated proportions of negative probes detected. Consequently, **a total of 1,561 cells (0.5%) were excluded during QC processes, leaving 301,597 cells available for downstream analysis**. Following the quality control procedures, it was noted that the WT samples exhibited a higher cell count possessing an increased number of Tx compared to the TG group (Fig. 3b).

Spatial transcriptomics platforms consistently performed with the mouse brain

In evaluating the concordance between two distinct platforms regarding their ability to recapitulate the biological characteristics of specimens, we performed a comparative analysis of expression levels by aggregating Tx or gene counts at the specimen level in RSC (see Methods). A curated list comprising 105 common gene symbols was extracted from two distinct gene panels, and the respective profiles were organized into subsets accordingly for further analysis. Initial investigations focused on assessing the correlation *between* consecutive specimens in terms of the aggregated count of each segment in the GeoMx DSP platform and the total Tx counts of all cells in the Xenium platform. The findings revealed a lowered consistency in the correlation of aggregated counts across AOIs and cells for the GeoMx DSP

and Xenium profiles (Fig. 3c). Notably, the WT group exhibited higher correlation coefficients than the TG group. Subsequent analyses were directed at calculating correlation coefficients *across* specimens, revealing that the majority of genes maintained consistent expression levels. However, an exception was noted for *Acta2*, which demonstrated a negative correlation (Spearman rho=−0.145), attributed to its low sensitivity. The mean and SD (standard deviation) of the summed expression for Xenium was recorded at 207.83 ± 162.3 in contrast to 28.33 ± 12.5 for GeoMx DSP. Despite this variance, *Acta2* was observed to retain its biological relevance with the summed count for the WT group surpassing that of the TG group in both profiles although the differences did not achieve statistical significance.

Both spatial platforms confirmed the WT-specific genes in PV interneurons

In our investigation, we performed the Wilcoxon rank-sum test to analyze differential expression patterns in our dataset, identifying a total of 37 differentially expressed genes (DEGs) with 31 and six showing decreased and increased expression, respectively, in TG compared to WT (Fig. 3d). Among the downregulated DEGs, three genes—*Dner*, *Gad1*, and *Pvalb*—were previously recognized as $M1^{PV}$ MAGs, whereas *Nrn1* and *Slc17a7* were identified as the $M3^{PV}$ MAGs. In contrast, *Gfap*, noted for its upregulation, was the only gene linked to both $M2^{PV}$ and $M3^{PV}$ MAGs. Given the limitations associated with Xenium technology, precisely its inability to perform segmentation like the GeoMx DSP and thus provide cell-type annotations, we ran unsupervised clustering to categorize cells based on their expression profiles obtained from Xenium. Through this approach and subsequent nonlinear dimensionality reduction for visualization purposes (Fig. 3e and see Methods), we successfully clustered 1.6% (158 out of 9,911) of the cells into a distinct group, referred to as Cluster 1 (*C1*). Even though cells are close together in the original high-dimensional space based on their features, a nonlinear dimensionality reduction technique does not preserve global distances or cluster shapes. Resulting cells from the same high-dimensional cluster may appear spread out or split into multiple disconnected clusters in 2D space. Subsequent differential expression (DE) analysis between *C1* cells and the remaining cell population revealed 26 and 48 genes to be down- and up-regulated in *C1*, respectively. Notably, the previously identified genes (*Dner*, *Gad1*, and *Pvalb*) were again significantly upregulated in *C1*, corroborating our initial findings. These genes exhibited a higher expression level in *C1* cells compared to other clusters (Fig. 3f). Further analysis was conducted to ascertain the expression patterns of the three significant genes in RSC, utilizing the Xenium Browser (v3.1.0) for spatial localization (Fig. 3g). As anticipated, expression was predominantly observed in *C1* cells across both TG and WT samples, with a notably higher proportion of *C1* cells present in WT compared to TG (Fig. 3h).

Higher correlation genes across specimens were successfully validated

Utilizing the GeoMx DSP for data analysis, it was determined that $M1^{PV}$ and $M2^{PV}$ exhibit associations with WT and TG, respectively. However, the limited quantity of genes within the Xenium panel and DEGs (Fig. 3d) introduces a challenge in validating the MAGs. A noteworthy limitation was the absence of overlap between $M2^{PV}$ MAGs and the DEGs; hence, the findings from the GeoMx DSP data analysis were not checkable (Supplementary Fig. S4). To address the limitations, the study engaged NMF results with 2000 features as a cell-type reference for the deconvolution of the Xenium profile. Utilization of the *W* matrices derived from PV and NeuN at designated ranks of three and four, respectively, provided a structured reference framework with 81 intersect genes in total (Fig. 4a and see Methods). As anticipated, the prevalence of $M1^{PV}$ cells was higher in WT, whereas $M2^{PV}$ cells predominated in TG. The analysis highlighted that due to the restricted range of features within the Xenium panel genes, the cell type inferred as PV cells exhibited an overly inclusive nature compared to the NeuN-inferred cells. Nonetheless, 118 (75%) out of 158 *C1* cells identified through unsupervised clustering were inferred as $M1^{PV}$ cells (Fig. 4b). To confirm the study's findings, DE analysis was conducted using a two-sided Wilcoxon rank-sum test and we identified 28 up-regulated genes in $M1^{PV}$ cells; three of them—*Dner*, *Gad1*, and *Pvalb*—were significantly differentially expressed between $M1^{PV}$ cells and the remaining cell populations (Fig. 4c). Within the context of $M2^{PV}$ upregulated genes, *Gfap* was identified as the only $M2^{PV}$ MAG within the Xenium panel. Regarding $M3^{PV}$ MAGs, three of them (*Gfap*, *Nrn1*, and *Slc17a7*) were included within the Xenium panel, where only *Nrn1* emerged as a DEG. **The correlation analysis across consecutive specimens for *Gfap*, *Nrn1*, and *Slc17a7* yielded coefficients of 0.54, 0.32, and 0.2, respectively. In contrast, the correlation coefficients for *Dner*, *Gad1*, and *Pvalb* were notably higher, recorded at 0.71, 0.81, and 0.77, respectively.**

Differentially expression analysis in five different brain sections revealed gene specificity

Unlike GeoMx DSP data (ROI selection, then profiling), the Xenium platform facilitated the profiling of entire tissue sections. Consequently, we expanded our study to include four additional brain sections within each specimen, namely the subiculum (**SUB**), visual cortex (**VIS**), entorhinal cortex (**ENT**), and the **CA1** region of the hippocampus (Fig. 4d and Supplementary Fig. S5). Apart from the RSC, a comprehensive selection of 14,289 cells was made from four distinct sections across the specimens. However, the SUB and VIS sections from the TG3F specimen and the SUB section from the TG4F specimen were absent from the selection due to the section loss. Subsequent dimensionality reduction analysis of the five regions revealed a unique pattern specific to the CA1 section and a distinct

subpopulation within the RSC or ENT cells (Fig. 4e). To validate the specificity of our observations in the RSC, DE analysis was conducted for each brain section to facilitate a comparative study between the TG and WT groups (Fig. 4f). Notably, ***Pvalb*** **exhibited the lowest Log2FC in the RSC, signifying a significant upregulation in the WT group. Similarly,** ***Dner*** **demonstrated upregulation in the WT group with the lowest Log2FC among the five sections analyzed.** On the other hand, the observation that *Gad1* in the VIS section displayed the lowest Log2FC suggests that it is not exclusive to the RSC, and the Log2FC difference between RSC and VIS was not greater than the differences of the other genes.

Subsequent validation of candidate biomarkers

We undertook a series of follow-up experiments incorporating both transcriptomic and proteomic assays to rigorously validate the down-regulated genes identified in the TG model in RSC through our spatial transcriptomics analysis (Fig. 5a). Our integrative analysis utilizing the GeoMx DSP and the Xenium In Situ platforms allowed us to identify three potential biomarkers that exhibited consistent and spatially distinct expression patterns across both datasets. Notably, these genes demonstrated differential expression patterns within PV+ cells, suggesting their potential functional relevance in the context of Alzheimer's disease pathology. Additionally, we included *Cox6a2*, a gene previously documented in the literature to be associated with vulnerability to Alzheimer's disease. This gene was identified as one of the $M1^{PV}$ MAGs but not captured by the Xenium platform due to inherent limitations of the gene panels used. Although the fourth candidate could not be analyzed at the single-cell resolution afforded by the Xenium platform, its inclusion enabled us to contextualize previously published findings within our tissue-specific framework.

To validate the transcript-level expression of the selected biomarkers, **we employed RNAscope in situ hybridization on RSC sections derived from both WT and TG groups** (Fig. 5b and see Methods). Gene-specific probes targeting *Pvalb, Gad1, Dner*, and *Cox6a2* were utilized, analyzing four to five biological replicates for each condition. The RNAscope results confirmed the spatial expression patterns previously identified in spatial transcriptomics datasets. Notably, *Pvalb* exhibited a significantly down-regulated signal (two-sided Welch's *t*-test, *P*-value=0.0075), corroborating its predicted localization as indicated by the GeoMx and Xenium data (Fig. 5c and Supplementary Fig. S6). Additionally, *Cox6a2*, which was identified through literature and absent from the Xenium panel, also demonstrated down-regulation (*P*-value=0.0035), thereby reinforcing its biological relevance. Furthermore, *Dner* (*P*-value=0.026) and *Gad1* (*P*-value=0.0367) also both showed impaired expression in PV+ interneurons of

TG mice. Collectively, these findings provide transcript-level validation for the candidate biomarkers and underscore their spatial specificity within the RSC.

To evaluate whether the transcript-level expression of the candidate biomarkers corresponded with protein-level alterations, **immunohistochemistry (IHC) was performed on matched tissue sections** (Fig. 5d and see Methods). Using validated antibodies targeting Pvalb, Gad1, Dner, and Cox6a2, we conducted staining across five independent biological replicates per condition (Fig. 5e and Supplementary Fig. S7). The IHC results largely reproduced the findings from RNAscope, revealing a down-regulation of Pvalb in the TG group (*P*-value=0.002), suggesting a maintained mRNA-to-protein correspondence. For Dner (*P*-value=0.0055) and Gad1 (*P*-value=0.0139), both RNAscope and IHC analyses supported differential expression across conditions; however, the level of statistical significance was notably enhanced in the protein-level assessment. This increase in signal strength and significance at the protein level may reflect factors such as enhanced protein stability, accumulation, or more robust antigen-antibody interactions, suggesting that Dner may play a more prominent functional role at the protein level in PV+ cells. Conversely, Cox6a2 exhibited a decrease in significance (*P*-value=0.0243).

We mapped their known biological functions onto a conceptual pathway to gain mechanistic insights into how the identified biomarkers may contribute to AD vulnerability (Fig. 6). The mitochondrial gene *Cox6a2* was significantly down-regulated in TG, suggesting impaired mitochondrial respiration and energetic stress (Fig. 6a). *Pvalb*, encoding parvalbumin, a calcium-binding protein essential for fast-spiking interneurons, showed reduced expression, which may reflect a loss of firing fidelity in these inhibitory neurons (Fig. 6b). Consistent with this, *Gad1* was also downregulated, indicating compromised synaptic inhibition (Fig. 6c). Finally, *Dner*, a Notch-related transmembrane protein involved in dendritic growth and maintenance, showed decreased expression in PV+, implying structural vulnerability through dendritic atrophy (Fig. 6d). Collectively, these markers illustrate a multi-level dysfunction that encompasses energy metabolism, interneuron excitability, synaptic inhibition, and neuronal structure, all of which may interact to exacerbate circuit instability associated with AD.

Integration with public datasets.

To place our findings in the context of prior work and to benchmark the direction of our effects against independent cohorts, we compared our results to published single-cell and spatial transcriptomic datasets. We used these datasets to assess whether PV-marker changes reported across studies show

consistent sex- and stage-related patterns. To integrate our findings with existing datasets, we analyzed three external resources: a STARmap mouse cortex and hippocampus dataset[27], a 10x Genomics Xenium dataset from the RSC[28], and the Brainmap SEA-AD consortium (human tissue from Brodmann area A9)[29,30]. In the STARmap dataset from Zeng et al.[63] we analyzed *Pvalb* and *Gad1* expression in PV-INs in the cortex and hippocampus of TauPS2APP Alzheimer's disease model mice. This data set was exclusively male mice. We observed (Supplementary Figu. S8a) a small decrease in the expression of *Pvalb* in the cortex that continued to decrease in older mice (8 months versus 13 months). *Gad1* expression within these cells appeared to decrease only in the older mice. To specifically examine retrosplenial cortex in another data set we utilized public Xenium spatial transcriptomics data from 10X Genomics. In male tgCRND8 mice, we observed little directional change in *Pvalb*, *Gad1* or *Dner* expression in 5.7-month transgenic mice but a later decrease in *Pvalb* expression in aged (17.9 month) male tgCRND8 mice (Supplementary Fig. S8b). Finally, in the BrainMap SEA-AD dataset, we observed the expected directional change in *Pvalb* expression in female AD patients, but no apparent change in male AD patients (Supplementary Fig. S9). This comparison was carried out in Brodmann area A9 (prefrontal cortex) as RSC data was not available.

Discussion

Spatial transcriptomic analyses are becoming increasingly accessible and are being applied to diverse questions across many platforms. This has the potential to provide insights on the diversity of cell types and the spatial relationships between them; however, it is important to keep in mind the strengths and limitations of the various spatial transcriptomic platforms. In leveraging the immunohistochemistry-guided bulk RNA sequencing of the Nanostring GeoMx DSP platform for the unbiased identification of subpopulations of PV+ neurons in the RSC of a mouse model of AD, we were able to identify the transcriptomic signatures of disease-associated PV+ neurons. These signatures were then used to assess the distribution of AD-associated PV+ cells across the RSC by using their expression profiles to guide the classification of single cell Xenium In Situ data and examine differences in their proportional representation and spatial distribution. Additionally, we assessed DEGs across the RSC using both platforms and report a high degree of coherence between these sets of results, providing robust support for impaired PV+ neuron populations within the RSC in AD. These findings underscore the heterogeneity of PV+ populations in the RSC during AD pathogenesis and offer potential molecular targets for therapeutic intervention.

One of the key findings of our study is the identification of PV+ interneuron-specific metagenes that exhibit differential expression patterns in AD. Our results indicate that PV+ interneurons in the RSC are not a homogeneous population but rather display distinct molecular subtypes, each with unique vulnerability to AD-related metabolic stress. The presence of metagenes specifically enriched in TG or WT mice suggests a potential mechanism through which these neurons undergo functional decline in AD. Notably, the differential expression of genes involved in synaptic function, neuronal excitability, and apoptotic regulation highlights potential pathways through which PV+ interneurons contribute to the dysregulation of cortical networks in AD. Our results also highlight the critical role of Cox6a2, Pvalb, Gad1, and Dner as key PV+ interneuron markers that are significantly downregulated in AD. The convergence of these molecular alterations points to a cascade of dysfunctions that may render specific neuronal populations more susceptible to degeneration in Alzheimer's disease. Reduced **Cox6a2** expression may impair oxidative phosphorylation[42], leading to bioenergetic failure in metabolically demanding neurons, such as PV+ interneurons. Compounding this, our metagene analyses identified decreased expression of *Gapdh*[43], *Ldhb*[44], and *Pgk1*[45] in PV+ interneurons in the RSC of TG mice, reducing the efficiency of glucose metabolism by these cells. Impaired lipid metabolism, through the down-regulation of *Pltp*[46], could further burden the bioenergetic functions of these cells. Together, these impairments place considerable strain on mitochondrial, wherein decreased expression of *Cox5a*[47], *Ndufa11*[48], and *Iscu*[49] cause further impairment to their function (Supplemental Table S1). This mitochondrial deficit could compromise the fast-spiking ability of these cells, as suggested by the concurrent downregulation of **Pvalb**, which is critical for calcium buffering and action potential timing[50]. Furthermore, we have previously demonstrated that many of the potassium channels, such as *Kcnip2*[51,52] and *Kcnc1*[53], which are critical for the maintenance of fast-spiking activity in PV+ interneurons are downregulated in the RSC of female 5xFAD mice[13]. These genes have also been identified in the current metagene analysis as being down-regulated in vulnerable PV+ interneuron populations (Supplemental Table S1). Together, this combination of alterations affecting fast-spiking properties align with electrophysiological characterization of RSC PV+ interneurons in female 5xFAD mice, wherein a sub-population of these cells displays impaired firing in response to current injection[13]. The loss of interneuron fidelity likely contributes to decreased GABAergic output, further supported by reduced **Gad1**[54] expression, resulting in diminished synaptic inhibition. Reductions in synaptic inhibition have previously been shown in RSC pyramidal cell populations of female 5xFAD mice, wherein these cells are hyperexcitable in response to current injection[13]. Furthermore, the amplitude of spontaneous inhibitory post-synaptic currents acting on pyramidal cells in de RSC are decreased in

female 5xFAD mice[13]. Consequently, impaired synaptic inhibition and resulting pyramidal cell hyperexcitability contributes to increased network excitability[55]—a hallmark of early AD pathology. Additionally, downregulation of **Dner** implies dendritic simplification or retraction, aligning with previous reports of decreased density of synaptotagmin-2 puncta, a marker of presynaptic contacts from PV+ interneurons, in the RSC of female 5xFAD mice[13]. These changes in synaptic density and integrity may further weaken synaptic integration and circuit connectivity[56]. These findings align with previous studies[57,58] that have implicated reduced GABAergic signaling in the progression of AD-related cognitive decline.

Interestingly, our multi-platform single-cell transcriptomic analysis revealed that impairments of these metabolic, electrophysiological, GABAergic, and synaptic markers was not uniform across all PV+ interneurons, suggesting that specific subpopulations may be more resilient to AD pathology. These results coincide with previously published functional analyses from 6-month-old female PV+ interneurons. In that study, we identified that approximately half of the PV+ interneurons showed impaired activity while the other half appeared to have normal properties[13]. In addition to providing context to the heterogeneity in the functional presentation of PV+ subpopulations in AD, the identification of markers of vulnerable and resilient cell populations enables the development of increasingly targeted interventions. With further advances in *in vivo* genetic manipulations, techniques such as *Pertub-seq*[59] could usher future treatment approaches. As the screening capacity of *Perturb-seq* steadily increases, comprehensive lists of metagene-identified vulnerability markers, such as those in the current study, can be used to identify vulnerable subpopulations *in vivo* and promote the physiological expression of these genes in a targeted manner. Targeted treatment approaches, enabled by the identification of subpopulations based on markers which can be screened for, moves the treatment of a highly heterogenous disease such as AD closer to the ideal of personalized medicine and improve treatment outcomes.

While these analyses have the potential to improve how subpopulations of given cell types are identified, classified, and treated in disease models, it is important to acknowledge limitations that affect the analyses of these data. In the current analyses, an arbitrarily selected threshold of Spearman rho > 0.5 was applied to binarize metagene correlation matrices to generate networks. Therefore, the organization of these metagene clusters may vary slightly under different thresholding criteria[60]. In addition, the correlation-based approach underpowers the detection of alterations in rare cell types or minor transcriptional changes. On the technical side, despite the extensive panel of barcodes in the Nanostring GeoMx Mouse Whole Transcriptome Atlas, the much smaller panel of genes in the Xenium

Mouse Brain Expression Panel (10X Genomics, 1000462) limited the intersection between these panels and reduced the breadth of the transcriptional profiles used for cell-type identification. With very nuanced differences between subpopulations, this may limit the ability to discern between single cell identities. In addition, GeoMx lacks single-cell resolution and cannot map transcriptional profiles back to exact tissue locations. Although we identified meaningful metagenes, we could not determine their enrichment in specific subtypes or spatial microenvironments. On the other hand, we did not perform cell-typing inference in the Xenium dataset due to the limited number of interneuron- and neuron-specific marker genes represented in the panel, which would hinder reliable classification of neuronal subtypes. However, while this limitation had the potential to impact the current study, spatial transcriptomic panels are continuously improving. Newly announced Xenium Prime 5k assays contain panels of 5,006 genes, allowing for much deeper characterization of cell types and enriching the potential for intersection between GeoMx and Xenium panels.

One of the secondary objectives of this study was to profile amyloid plaques within AD cohorts to potentially enable a deeper molecular and spatial characterization of these pathological features. However, a notable limitation emerged during quality assessment: all amyloid-targeted AOIs failed to meet the criteria required for downstream analysis. This issue can be attributed to a key biological property of amyloid plaques which is that they are extracellular protein aggregates rather than cellular structures. Despite covering a relatively large area on tissue sections, these regions often present with low or negligible nuclei counts. This discrepancy poses a challenge in spatial transcriptomic platforms like GeoMx DSP, where nucleus-based quality metrics and RNA content are critical for inclusion.

We validated gene expression in TG mice using RNAscope and IHC techniques on tissue samples from separate groups of 5xFAD and WT mice. Additionally, we performed an in-depth search for publicly available datasets using other spatial transcriptomic technologies in mouse models of AD which could be leveraged for further validation. This search included PubMed indexing of four Medical subject Headings (MeSH) terms – Alzheimer's Disease, Mice, Transcriptome, and Gene Expression Profiling – to comprehensively identify relevant studies published within the past five years. While 564 articles met these criteria (as of May 15, 2025), only 26 of these publications were accessible and provided associated data. Upon manual review, most of these data sets exclusively profiled gene expression in male mice[61], wherein we have previously shown that the PV+ interneurons of the RSC are more resilient to AD pathology than in female mice[13]. Secondly, in studies where both male and female mice were examined, profiling was largely focused on other regions, such as the hippocampal subregion

CA1[62]. While these complications limited the utility of published datasets in validating the unique data analyzed in the current study, this further emphasizes the importance of our data.

The findings of the present study align with a growing body of transcriptomic and spatial-omics literature demonstrating that Alzheimer's disease (AD) is characterized by highly localized, cell-type–specific molecular alterations rather than uniform transcriptional shifts across entire brain regions[16, 63-66]. Several spatial transcriptomic studies have emphasized plaque-centered molecular changes, identifying concentric gene-expression programs dominated by oligodendrocyte, inflammatory, and lysosomal pathways that emerge and evolve with increasing amyloid burden[61]. High-resolution in situ approaches further refined this framework by revealing structured plaque microenvironments composed primarily of glial and immune-associated cell states[66], a view reinforced by publicly available spatial datasets showing progressive transcriptional remodeling that parallels plaque accumulation over time. While these studies have provided important insight into plaque-associated molecular organization, their plaque-centric focus can limit detection of neuron-intrinsic transcriptional changes, particularly within relatively rare but functionally critical neuronal populations such as inhibitory interneurons.

In contrast, the current study demonstrates that parvalbumin interneurons (PV-INs) in the retrosplenial cortex (RSC) exhibit pronounced transcriptional heterogeneity in AD, with discrete metagene-defined subpopulations showing selective vulnerability. By integrating GeoMx DSP and Xenium In Situ spatial transcriptomics, we show that PV-INs segregate into distinct transcriptional states that differ by genotype and display minimal gene overlap, consistent with discrete molecular identities rather than graded disease-related shifts. This observation extends prior work demonstrating that inhibitory neurons, and PV interneurons in particular, engage AD-associated transcriptional programs earlier than excitatory neurons[13, 15, 67]. Notably, disease-associated PV metagenes were detectable independently of plaque-targeted sampling, suggesting that PV-IN vulnerability does not strictly require immediate plaque proximity. The transcriptional features defining vulnerable PV subpopulations converge on metabolic, electrophysiological, inhibitory, and structural pathways, including coordinated downregulation of *Cox6a2*, *Pvalb*, *Gad1*, and *Dner*. These findings are consistent with prior proteomic and transcriptomic studies showing that PV-INs are metabolically demanding, enriched for mitochondrial and fast-spiking gene programs, and particularly sensitive to energetic stress[13,15,68]. Our data extend this framework by demonstrating that these impairments are restricted to specific PV

subpopulations, providing a molecular explanation for the partial and heterogeneous PV dysfunction reported in electrophysiological and circuit-level studies.

Concordance with published datasets.

Across independent datasets, PV-marker changes generally align with our current and previously published findings and support a model in which PV-INs become progressively dysregulated in AD, with modulation by sex, age, and brain region. In this framework, vulnerability emerges earlier in females, particularly in the RSC, followed by later involvement of males and additional regions as pathology advances. Consistent with this pattern, SEA-AD[29,30] shows a female-specific reduction of *Pvalb* in the human cortex, while male-only mouse datasets suggest either gradual age-dependent declines[27] (TauPS2APP; with *Gad1* changes more evident later) or minimal early change followed by reduced *Pvalb* in aged RSC (TgCRND8 Xenium)[28]. While generally consistent with our overarching theme of AD-induced PV-IN dysfunction, it is important to acknowledge some of the limitations of these datasets. Inference is constrained by male-biased rodent datasets, sparse RSC sampling inconsistent age-matching and by small cohorts (e.g., n = 1–2) that required treating individual cells as replicates. Due to these limitations statistical significance or lack thereof should be viewed as suggestive rather than definitive. Overall, by combining RSC-focused cell-type resolution, cross-platform validation within a single experimental framework, and explicit consideration of sex and disease stage, the current work extends what could be inferred from heterogeneous, limited-cohort resources and clarifies how PV-marker changes relate to a coherent, region-relevant AD vulnerability profile.

Lastly, it is important to acknowledge the limitations of the 5xFAD mouse model in the context of our findings. Although this model is widely used due to its robust and early-onset amyloid pathology, it does not fully recapitulate the multifactorial nature of Alzheimer's disease. Notably, 5xFAD mice lack tau neurofibrillary tangle formation. and is driven by genetic mutations and exhibits a rapid disease course, which may not reflect the slower and more heterogeneous progression of sporadic, late-onset AD in humans. Future studies will be necessary to validate these transcriptional signatures in human tissue. However, in our previous work[13] we have identified that PV+ interneuron loss is observed in the RSC of human AD patients suggesting the basic vulnerability of these neurons extends from our mouse model into disease populations.

In conclusion, we identified heterogeneity in PV+ transcriptional profiles across the RSC in a mouse model of AD, revealing differentially vulnerable and disease-associated transcriptional profiles among

these cells. The outlined integration of GeoMx DSP and Xenium In Situ provides not only insight into the vulnerability of PV+ neurons during AD pathogenesis but also provides a framework for the generation of disease and cell-type specific cell-type identity inferences in spatial transcriptomic analyses.

Methods

Mice and sample preparation

All animal experiments were carried out in accordance with the guidelines set by the Canadian Council on Animal Care and were approved by the University of Calgary Animal Care Committee. Female heterozygous 5xFAD (TG) mice and their transgene-negative wild-type (WT) littermates were used for all analyses. All mice were 6 months old at the time of tissue collection. Mice were bred via in vitro fertilization at the University of Calgary Centre for Genome Engineering. Sperm was collected from a male 5xFAD breeder (#034840-JAX) and oocytes were obtained from C57Bl/6J females (#000664-JAX), all of which were obtained from The Jackson Labs. The mice were housed under standard conditions with three to five mice per cage and had free access to food and water. The lighting was maintained on a 12-hour light/dark cycle with lights on at 8 a.m in a room with with controlled temperature and humidity. At 6-month-old, mice were deeply anesthetized with isoflurane and transcardially perfused with 0.1 M phosphate-buffered saline (PBS) and 4% formaldehyde. Following perfusion, brains were removed and postfixed in 4% formaldehyde for 24 h at 4°C prior to paraffin embedding.

GeoMx digital spatial profiler data acquisition

The NanoString GeoMx DSP (Digital Spatial Profiler) assay was performed according to the manufacturer's protocol (NanoString, Inc., MAN-10150), using the Mouse Whole Transcriptome Atlas (WTA). This atlas contains 20,175 probe targets and provides next-generation sequencing (NGS) as the readout.

Tissue preparation and hybridization: Formalin-fixed paraffin-embedded (FFPE) brains were hemisectioned at a thickness of 5 μm and mounted to a plain glass slide. For these experiments, female WT (*N*=3) and TG (*N*=4) mice were used. Sections were deparaffinized with xylene and subjected to antigen retrieval (Tris-EDTA, pH 9, 20 min at 98°C) followed by Proteinase K digestion (0.1 μg/mL, 15 min at 37°C). Sections were incubated overnight at 37°C with WTA probes diluted in hybridization buffer R for 18 hours.

Immunostaining and imaging: The following day, sections were washed twice with a solution of saline-sodium citrate (SSC)/50% formamide (25 min per wash at 37°C), blocked with buffer W (30 min at room temperature), and incubated with a solution containing 1:100 Alexa Fluor 488-conjugated anti-NeuN antibody (Sigma-Aldrich; ABN78A4), 1:100 Alexa Fluor 594-conjugated anti-PV antibody (in-

house conjugation; Abcam ab269822, Invitrogen PA1-933), and 1:50 SYTO 83 (Thermo Fisher, S11364) in buffer W for 1 h at room temperature. Sections were briefly washed in SSC and scanned at 20X magnification using the GeoMx DSP platform.

Barcode collection and sequencing: Areas-of-illumination (AOIs) were defined within ROIs in the RSC based on morphological markers, including PV, NeuN, and Amyloid. Each ROI could contain up to four AOIs corresponding to distinct cellular features: PV+ interneurons, NeuN+ neurons, Amyloid+ plaques, and triple-negative (TN) regions lacking all three markers (PV−/NeuN−/Amyloid−) (Supplementary Table S4). Spatially resolved gene expression profiling was achieved by illuminating the selected AOIs with UV light to release oligonucleotide barcodes from hybridized probes. Barcodes were collected using microfluidics and deposited in separate wells of the GeoMx DSP collection plate. Following sample barcode retrieval, PCR amplification was performed to incorporate unique Illumina i5 and i7 dual indices.

Library preparation and data processing: PCR products were purified twice with AMPure XP beads (Beckman Coulter, A63881) and quantified using a Qubit fluorometer (Thermo Fisher Scientific). Library quality was assessed using a Bioanalyzer (Agilent Technologies). For whole transcriptome analysis, the target sequencing depth was 100 counts/μm². Sequencing was performed on an Illumina NovaSeq, and FASTQ files were processed into gene count data using the Nanostring GeoMx NGS Pipeline (v3.1.1.5; Nanostring, Inc., MAN-10153).

Xenium In Situ data acquisition

Tissue preparation and hybridization: TG and WT brains were hemisectioned at 5 μm thickness and prepared following the recommendations outlined in the Xenium In Situ for FFPE Tissue Preparation Guide (10x Genomics, CG000578). Brain sections from female TG (*N*=3) and WT (*N*=3) mice were mounted on Xenium slides, deparaffinized, and permeabilized to expose mRNA. Following the Xenium In Situ Gene Expression protocol (10x Genomics, CG000582), hybridization was performed overnight at 50 °C using the Xenium Mouse Brain Gene Expression panel (10x Genomics, 1000462). This panel contains 247 probes, including two negative controls. Unhybridized probes were removed by washing, and the remaining hybridized probes were ligated to their specific mRNA targets during a 2-hour ligation step at 37 °C. To enhance detection, rolling circle amplification was performed for 2 hours at 37 °C. Following amplification, slides were washed, background fluorescence was chemically quenched, and a DAPI stain was applied to aid in subregion identification.

Imaging and analysis: All instrument-specific reagents and buffers were prepared according to the Xenium Analyzer User Guide (10x Genomics, CG000584). The Xenium slides were loaded onto the Xenium Analyzer platform, alongside the required reagents and buffers for automated in situ analysis. An initial scan of the tissue sections allowed the identification of regions of interest across the full section, which were selected using the Xenium Analyzer software. With regions of interest defined, slides underwent multiple rounds of image acquisition. During each cycle, fluorescently labelled oligonucleotides specific to the amplified probes were hybridized, imaged, and then removed, generating optical signatures corresponding to each gene-specific barcode. These signatures were later decoded into gene identities. Only transcripts with a Xenium Quality Value >20 were retained for further analysis. Images were captured with an XY localization precision of <50 μm and Z-stacks were collected with a step size of 0.75 μm across the entire tissue section. Stitched images provided a high-resolution spatial map of transcripts throughout the brain sections. Data were processed locally using the standard 10x Genomics Xenium workflow, producing both cell-by-gene and transcript-by-location matrices, enabling comprehensive spatial transcriptomic analysis.

GeoMx DSP data preprocessing

The quality assessment of the GeoMx DSP data was conducted following the guidelines from the R package *GeomxTools* (v3.8.0) (https://www.bioconductor.org/packages/release/workflows/vignettes/GeoMxWorkflows/inst/doc/GeomxTools_RNA-NGS_Analysis.html). Initially, we evaluated the sequencing quality for each AOI using the threshold values from the vignette. After the AOI segment QC, we performed probe-level QC using the Grubb's test (global outlier) and the count proportion of each segment via geometric mean (local outlier). Quantifications from multiple probes were then aggregated at the gene level. Subsequently, we calculated the background signal from negative probes to determine the limit of quantification (LOQ) per AOI segment and filtered out counts lower than LOQs. Samples with low coverage, where less than 10% of the genes were quantified genome-wide, were also filtered out. We did not utilize the upper-quartile normalization from the guidelines but instead applied the variance stabilizing transformation (VST) method using the R package *DESeq2* (v1.44.0)[31]. Principal component analysis was performed to identify potential outliers and assess the data properties using the *prcomp* function in the R package *stats* (v3.6.2), a default package. Finally, the GeoMx DSP data QC report and a set of codes are available online: https://bioinformatics.ucalgary.ca/publications/MM-in-PVIN/GeoMx/.

Identification of differentially expressed genes (DEGs)

Differential expression analysis was carried out using a two-sided Welch's *t*-test and Log2FC for a bulk RNA-seq, i.e., GeoMx DSP data, between two groups. DEGs were identified when an FDR was less than 0.05 and an absolute Log2FC was greater than 0.2. On the other hand, a two-sided Wilcoxon rank sum test was used using the R package *presto* (v1.0.0, https://github.com/immunogenomics/presto) for a profile at the single-cell level, i.e., Xenium data, and DEGs were identified when the adjusted *P*-value was less than 0.05 and the absolute Log2FC was greater than 0.5. A volcano plot was generated using the R package *ggplot2* (v3.5.1)[32], and the gene symbols were labelled using the R package *ggrepel* (v0.9.6, https://github.com/slowkow/ggrepel).

Nanostring GeoMx DSP data deconvolution

The analysis-ready expression profile was segmented into PV and NeuN, and each segment was processed separately. For each segment, we retained the original feature space while selecting a subset of relevant features. We identified the top 2000 highly variable genes based on a coefficient of variation (CV) greater than 0.01 and ordered them by the SD. The CV and SD were computed using the *cv* function in the R package *EnvStats* (v3.0.0)[33] and the *sd* function in the R package *stats* (v3.6.2), respectively. To identify biologically relevant transcriptional programs within PV and NeuN segment, we utilized an unsupervised approach, non-negative matrix factorization (NMF), with the R package *NMF* (v0.28)[33]. This approach facilitates the identification of distinct gene expression signatures known as metagenes. Each metagene corresponds to a coherent set of co-expressed genes that may indicate specific biological states or cell subtypes. We opted for NMF over alternative dimensionality reduction techniques because NMF imposes a non-negativity constraint which enhances interpretability in the context of gene expression data where negative values lack biological significance. This characteristic allows for a more intuitive understanding of how gene modules contribute to sample-specific expression profiles. When running NMF, we set the parameters as follows: *rank* = [2, 10], *method* = brunet, *iteration* = 1000, and *seed* = 123456. In NMF, the rank parameter determines the number of latent transcriptional programs, i.e., metagenes, used to represent the biological profile. Each metagene reflects a distinct pattern of gene co-expression that corresponds to a biological process, cellular state, or subtype. The rank can be interpreted as the resolution at which molecular heterogeneity is examined. For example, lower ranks may capture broad transcriptional programs shared across cell types, while higher ranks can reveal more specific gene expression modules including those associated with disease or cell-type-specific responses. A script for each rank was submitted to the job scheduler on HPC (high-performance computing) and the resulting NMF objects were merged into a single NMF object. This

NMF object consisted of two matrices at each rank: **(1) coefficient *H* matrix, where columns represent samples and rows represent metagenes**[24]**, and (2) basis *W* matrix, where columns and rows represent metagenes and genes, respectively.**

Select the optimal rank from the deconvolution

In our analysis, we performed matrix concatenation across different ranks to create metagenes clusters. We then utilized the R package *corrr* (v0.4.4, https://github.com/tidymodels/corrr) to compute the pairwise Spearman correlation coefficient across metagenes. Metagene pairs with a correlation coefficient greater than 0.5 were used to construct a correlation network using the R package *igraph* (v2.0.3)[34]. Subsequently, we identified biological modules using the *cluster_fast_greedy* function from the correlation network in each segment. For the NeuN segment, we additionally optimized the layout of the correlation network to enhance visualization. We determined the optimal number of latent factors, or rank, from the NMF results for downstream analysis by selecting the minimum rank that encompasses the most biological modules. Additionally, we labelled metagenes at each rank on the correlation network to assess the inclusion of communities in downstream analysis. Small (a couple of nodes) or sample-specific communities were excluded. The functions utilized in this study are available as part of the Spatial Omics Toolkit (SOTK), which is publicly accessible on GitHub: https://github.com/UC-ASOC/SOTK

Metagene-associated genes and functional annotation

We identified metagene-associated genes (MAGs) by extracting a list of genes from each metagene through the following steps: (1) selecting the top 100 genes based on the basis (*W* matrix), and (2) identifying genes that exhibited a Spearman rho >0.2 between the level of expression and coefficient values (*H* matrix) on a sample-by-sample basis for each metagene[36]. The MAGs were then used for enrichment tests using hypergeometric testing with GO (Gene Ontology, https://geneontology.org/), KEGG (Kyoto Encyclopedia of Genes and Genomes, https://www.genome.jp/kegg/) Pathway, and Reactome (https://reactome.org/) databases on g:Profiler[37] with a range of term sizes from 10 to 500.

Metagene-sample relationships

Based on the coefficient values (*H* matrix), each sample was assigned to a specific metagene based on the greatest coefficient value. Conversely, a single metagene could have multiple samples assigned as the coefficient values were compared within each sample. Visualization of the relationships between metagenes and samples was performed at a selected rank in each segment to investigate the overrepresentation of the metagenes in each sample.

Xenium In Situ data preprocessing and ROI selection

Xenium instrument performed quality assessment internally such as checking for out-of-focus FOVs (field of view) and outputting a single-cell profile with spatial information. We imported parquet and h5 files using the R package *arrow* (v17.0.0.1, https://github.com/apache/arrow/) and *HDF5Array* (v1.32.1, https://bioconductor.org/packages/HDF5Array). We ran the following steps to exclude low-quality transcripts (Tx) and cells: (1) Tx that are unassigned to any cells, (2) cells with a significantly large area were excluded because they are undersegmented (when more than one cells segmented as one) using the Grubb's test with the *grubbs.test* function in the R package *outliers* (v0.15, https://cran.r-project.org/web/packages/outliers), (3) cells with few (<10) Tx detected, and (4) cells with a significant amount of background signals from negative probes when the proportion of the negative probe detected is greater than 5%. Xenium, by default, includes high-quality Tx (20 phred quality score or greater, an error rate of 1 in 100) and we used the same threshold value. After QC, we compiled the profiles into a SingleCellExperiment object using the R package *SingleCellExperiment* (v1.26.0)[38] for each sample. Then, multiple objects were merged into a single object using the R package *scMerge* (v1.20.0)[39]. With the high-quality Xenium data, we used the Xenium Explorer (v3.1.0) to select the ROIs in five sections, namely RSC, VIS, SUB, ENT, and CA1, and subsetted cell IDs to subset the profiles of these regions.

Lastly, the Xenium data QC report with a set of codes is available online: https://bioinformatics.ucalgary.ca/publications/MM-in-PVIN/Xenium/.

Comparison of the level of expression between two Spatial Transcriptomics platforms

A comparative analysis of mRNA expression quantification was undertaken between two Spatial Transcriptomics platforms, which offer two distinct features: Xenium measures mRNA expression at the granularity of individual cells, while GeoMx DSP quantifies it as bulk RNA-seq. The inherent disparities between these platforms necessitated an approach whereby expression levels per specimen or gene were aggregated and subsequently analyzed to determine the correlation coefficients both between consecutive specimens and *across* the specimens[40]. Initially, the analysis was refined to encompass a subset of genes that were consistently represented across both the GeoMx DSP WTA and the Xenium Predesigned Mouse Brain panels. This subset excluded the specimen TG1F due to its absence in the Xenium data. In addition, we only included cells in RSC from Xenium data to fairly compare the two platforms. For each specimen, the aggregate Tx counts across cells per gene were calculated within the Xenium profile. In contrast, the GeoMx profile facilitated expression profiling at the AOI level in each segment. Subsequently, a Spearman correlation analysis was employed to assess the relationship *between* specimens with vectors of size equivalent to the gene count. Conversely, the aggregation of Tx or gene counts per specimen was computed to compare correlation across specimens (vector sizes reflecting the number of specimens involved).

Unsupervised clustering and nonlinear dimensionality reduction

In the GeoMx data analysis, an admixture signal was detected in PV and NeuN, but we successfully quantified the mRNA expression from the marker-based cells in each segment. The Xenium experiments were conducted without a segmentation, leading to the unavailability of cell type annotation. Therefore, we performed cell typing using *k*-means clustering with *k* set to seven based on the identification of three PV and four NeuN biological modules as minimum cell populations. This informed choice allowed us to partition the cells into biologically meaningful groups. *K*-means was performed using Euclidean distance to assign each cell to the nearest cluster centroid, and the algorithm iteratively refined the cluster assignments to minimize the within-cluster sum of squares. Following the *k*-means clustering, we applied t-SNE (t-distributed Stochastic Neighbor Embedding) using the R package *Rtsne* (v0.17, https://github.com/jkrijthe/Rtsne) with the default parameters and assigned cluster colours using the R package *RColorBrewer* (v1.1-3, https://CRAN.R-project.org/package=RColorBrewer). Lastly, we visualized the expression level in each cluster in a

violin plot for each Tx with the cluster and expression level represented on the X- and Y-axes, respectively. The expression level was transformed using the *asinh* function (hyperbolic arcsine of a value).

Cell type inference using the NMF basis matrices as a reference

The elucidation of interneuron- and neuron-specific markers remains a substantial challenge and eight PV-specific DEGs were recognized within the Xenium panel. To address this gap, we employed NMF outputs to infer cellular phenotypes from the generated data. Specifically, we concatenated two *W* matrices derived from NMF analyses at selected ranks, organizing the data such that rows represented features and columns corresponded to metagenes. This approach facilitated the deconvolution of the Xenium profile in the RSC employing the R package *InSituType* (v2.0)[41] developed by Nanostring. The *insitutypeML* function required three matrices: the Tx count matrix, negative control probes, and the reference set which was the concatenated *W* matrices. It is noteworthy that the deconvolution process was constrained by the limited gene overlap between the NMF features and the genes represented in the Xenium panel, while non-overlapping genes were ignored. *InSituType* executed a hard clustering algorithm, resulting in the definitive classification of each cell into a singular cell type.

Candidate gene validation

RNAscope procedures: The altered expression profiles of all four candidate genes (*Pvalb*, *Gad1*, *Dner*, and *Cox6a2*) were validated using RNAscope *in situ* hybridization. These validation experiments were performed using a second cohort of 6-month-old female heterozygous 5xFAD (*N*=4) mice and transgene-negative WT (*N*=5) littermates. Mice were deeply anesthetized with isoflurane and decapitated. Brains were rapidly dissected, submerged in Tissue-Tek® O.C.T. Compound (Sakura, 4583), frozen using dry ice and isopentane, and then stored at -80 °C. Brains were sectioned coronally at a thickness of 20 μm on a cryostat (Leica CM 1950, Concord, ON, Canada) and mounted directly to charged slides (SUPERFROST® PLUS Gold Slides, Electron Microscopy Sciences, 71864). Slides were stored in sealed slide holders and kept at -80 °C.

The slides were removed from -80 °C and immediately placed into the pre-chilled 4% PFA for 15 mins. Samples were subsequently washed with PBS and dehydrated with washes in 50%, 70% and 100% ethanol. Afterwards, samples were pretreated using protease III at 40 °C. After the steps of fresh-frozen sample preparation and pretreatment, the RNAscope Multiplex Fluorescent v2 assay (Advanced Cell Diagnostics, ACD, Cat. No. 323100) was used for the single-molecule detection of RNA targets by

following the manufacturer's protocol. Hybridize probes (Mm-Gad1-C1, 400951; Mm-Dner-C2, 413951-C2 or Mm-Cox6a2-C2, 461371-C2; Mm-Pvalb-C3, 421931-C3) were applied and TSA Vivid Dyes 520, 570 and 650 (ACD, 323271, 323272, and 323273) were used for C1, C2, C3 probes with the individual dilution ratio of 1:6000, 1:4000 and 1:4000, respectively. Finally, samples were counterstained with DAPI and coverslipped using ProLong™ Gold antifade mounting medium (Invitrogen, P36930).

RNA scope imaging and analysis: Tissue was imaged using an OLYMPUS FV3000 confocal microscope equipped with a 40X oil immersion objective (NA of 1.40). Volumetric scans (1.5X zoom; 60x total magnification; 0.42 μm z spacing) were collected from the RSC, with approximately 30 cells being imaged per mouse across two to three sections each. These images were loaded into ImageJ where maximum intensity projections were generated for each cell. Cells were traced based on *Pvalb* RNA labelling and the presence of a DAPI-labelled nucleus. Within each traced cell, mean intensity of each fluorescent channel was assessed as a proxy of transcript expression.

Immunohistochemistry procedures: To assess the impact of altered transcriptional profile on downstream protein expression, the expression of Pvalb, Gad1, Dner, and Cox6a2 proteins were assessed using IHC. These validation experiments were performed using a third cohort of 6-month-old female heterozygous 5xFAD (*N*=5) mice and transgene-negative WT (*N*=5) littermates. Mice were deeply anesthetized with isoflurane and transcardially perfused with PBS and 4% formaldehyde. Brains were extracted and postfixed in 4% formaldehyde for 24 h before cryoprotection in 30% w/v sucrose solution in PBS for 24 – 48 h. Brains were sectioned at a thickness of 50 μm on a cryostat in 12 series and stored at -20 °C in a buffered antifreeze solution containing 30% ethylene glycol and 20% glycerol in PBS. °C.

Immunofluorescent staining of Gad1 (1:250, Mouse, ProteinTech, 67648), Dner (1:500, Goat, Invitrogen, PA5-47280), and Cox6a2 (1:500, Rabbit, ProteinTech, 11421) was performed across separated tissue series, with each label being accompanied by Pvalb (1:2000, Rabbit, Invitrogen, PA1-933; or 1:500, Chicken, Aves Lab 78-479-020). For all labels, tissue sections were washed three times (10 min per wash) in PBS. Sections were then incubated for 24 h in a primary antibody solution of primary antibody, 3% normal donkey serum, and 0.3% Triton X-100 in PBS. Following primary incubation, tissue was washed three times (10 min per wash) in PBS before incubation in a solution of 1:500 secondary antibody (Gad1: donkey anti-mouse Alexa Fluor 594, Jackson ImmunoResearch, 715-585-150; Dner: donkey anti-goat Alexa Fluor Plus 555, Invitrogen, A32816; Cox6a2: donkey anti-rabbit

Alexa Fluor 594, Jackson ImmunoResearch, 7111-585-152; Pvalb alpaca anti-rabbit Alexa Fluor 647, Jackson ImmunoResearch, 611-605-215; or donkey anti-chicken Alexa Fluor 647, Jackson ImmunoResearch, 703-605-155) in PBS for 24 h. Finally, tissue was counterstained with 4',6-diamidino-2-phenylindole (DAPI; 20 min, 1:1000 in PBS) and washed twice (10 min per wash) with PBS before being mounted to glass slides and coverslipped with PVA-DABCO mounting medium.

IHC imaging and analysis: Analyses of protein expression were conducted using images of the RSC were collected using an OLYMPUS FV3000 confocal microscope equipped with a 40X oil immersion objective (NA of 1.40). Volumetric images of 30 PV+ interneurons were collected per mouse, across an average of two to three sections, with a z-spacing of 0.45 μm. These images were loaded into ImageJ, and maximum intensity projections were generated corresponding with the bounds of each cell. Using Pvalb staining as a reference, cells were traced and the mean pixel intensity value for each immunofluorescent label of interest was assessed within these bounds as a proxy of protein expression level.

Statistics & Reproducibility

No statistical method was used to predetermine sample size. Sample sizes were determined based on the availability of age-matched female 5xFAD transgenic (TG) and wild-type (WT) littermate mice at 6 months of age,and were further constrained by the capacity of the GeoMx DSP and Xenium In Situ slides. For GeoMx DSP analysis, four TG and three WT mice were used, yielding 12 PV and 14 NeuN AOIs, respectively. For Xenium In Situ analysis, three TG and three WT mice were used. One PV AOI was excluded from GeoMx DSP analysis due to insufficient coverage, where less than 10% of genes were detected genome-wide. All remaining data passed quality control thresholds and were retained for analysis.

Data Availability

The GeoMx DSP and Xenium In Situ data generated in this study have been deposited in the GEO (Gene Expression Omnibus) under the accession numbers, respectively. GSE277793 (https:/www.ncbi.nlm.nih.gov/geo/query/acc.cgi?acc=GSE277793) and GSE277463 (https://www.ncbi.nlm.nih.gov/geo/query/acc.cgi?acc=GSE27746)
The processed data, NMF outputs, deconvolution/clustering results, are publicly available on Zenodo at https://doi.org/10.5281/zenodo.17834664.
SEA-AD 10x single nucleus RNA-seq data referred to in thus study are available through the AD Knowledge Portal (Synapse study **syn26223298**). STARmap PLUS data are available on Zenodo at https://doi.org/10.5281/zenodo.7332091 10X genomics Xenium TgCRND8 dataset is publicly available at
https://www.10xgenomics.com/datasets/xenium-in-situ-analysis-of-alzheimers-disease-mouse-model-brain-coronal-sections-from-one-hemisphere-over-a-time-course-1-standard
The source data used for all analyses in this study are provided in the Supplementary Information/Source Data file. All raw data associated with the manuscript are publicly available without restriction in the repositories listed above (spatial transcriptomics) or in the supplemental materials (ISH and IHC data).

Code Availability

We provide the code for our analysis framework, SOTK (Spatial Omics Toolkit), at https://doi.org/10.5281/zenodo.17834664 . Users can also demonstrate the SOTK with the GeoMx DSP data online at https://asoc.shinyapps.io/sotk/. In addition, the following software programs used for analysis and visualization are made available by Nanostring and 10x Genomics: *GeoMX NGS Pipeline* that converts FASTQ to DCC was shared by the Nanostring, and *Xenium Explorer* was used to capture cells and Tx in regions of interest is publicly available at https://www.10xgenomics.com/support/software/xenium-explorer/latest.

References

1. Edison, P. *et al.* Amyloid, hypometabolism, and cognition in Alzheimer disease: an [11C]PIB and [18F]FDG PET study. *Neurology* **68**, 501–508 (2007).
2. Groot, C. *et al.* Differential trajectories of hypometabolism across cognitively-defined Alzheimer's disease subgroups. *NeuroImage Clin.* **31**, 102725 (2021).
3. Kim, D. K. & Mook-Jung, I. The role of cell type-specific mitochondrial dysfunction in the pathogenesis of Alzheimer's disease. *BMB Rep.* **52**, 679–688 (2019).

4. Nestor, P. J., Fryer, T. D., Ikeda, M. & Hodges, J. R. Retrosplenial cortex (BA 29/30) hypometabolism in mild cognitive impairment (prodromal Alzheimer's disease). *Eur. J. Neurosci.* **18**, 2663–2667 (2003).

5. Terstege, D. J., Galea, L. A. M., Epp, J. R. & Alzheimer's Disease Neuroimaging Initiative. Retrosplenial hypometabolism precedes the conversion from mild cognitive impairment to Alzheimer's disease. *Alzheimers. Dement.* (2024) doi:10.1002/alz.14258.

6. Ghirardini, E. *et al.* Cell-specific vulnerability to metabolic failure: the crucial role of parvalbumin expressing neurons in creatine transporter deficiency. *Acta Neuropathol. Commun.* **11**, 34 (2023).

7. Terstege, D. J. & Epp, J. R. Parvalbumin as a sex-specific target in Alzheimer's disease research - A mini-review. *Neurosci. Biobehav. Rev.* **153**, 105370 (2023).

8. Hu, H., Gan, J. & Jonas, P. Interneurons. Fast-spiking, parvalbumin^{+} GABAergic interneurons: from cellular design to microcircuit function. *Science* **345**, 1255263 (2014).

9. Inan, M. *et al.* Energy deficit in parvalbumin neurons leads to circuit dysfunction, impaired sensory gating and social disability. *Neurobiol. Dis.* **93**, 35–46 (2016).

10. Deleuze, C. *et al.* Strong preference for autaptic self-connectivity of neocortical PV interneurons facilitates their tuning to γ-oscillations. *PLoS Biol.* **17**, e3000419 (2019).

11. Walsh, C. *et al.* B bursting in the retrosplenial cortex is a neurophysiological correlate of environmental novelty which is disrupted in a mouse model of Alzheimer's disease. *J. Neurosci.* **42**, 7094–7109 (2022).

12. Park, K., Kohl, M. M. & Kwag, J. Memory encoding and retrieval by retrosplenial parvalbumin interneurons are impaired in Alzheimer's disease model mice. *Curr. Biol.* **34**, 434–443.e4 (2024).

13. Terstege, D. J. *et al.* Impaired parvalbumin interneurons in the retrosplenial cortex as the cause of sex-dependent vulnerability in Alzheimer's disease. *Sci. Adv.* **11**, eadt8976 (2025).

14. Guennewig, B. *et al.* Defining early changes in Alzheimer's disease from RNA sequencing of brain

regions differentially affected by pathology. *Sci. Rep.* **11**, 4865 (2021).

15. Chen, K. S. *et al.* Regional interneuron transcriptional changes reveal pathologic markers of disease progression in a mouse model of Alzheimer's disease. *bioRxivorg* 2023.11.01.565165 (2023).
16. gr, H. *et al.* Single-cell atlas reveals correlates of high cognitive function, dementia, and resilience to Alzheimer's disease pathology. *Cell* **186**, 4365–4385.e27 (2023).
17. Merritt, C. R. *et al.* Multiplex digital spatial profiling of proteins and RNA in fixed tissue. *Nat. Biotechnol.* **38**, 586–599 (2020).
18. Yau, H.-J., Wang, H.-F., Lai, C. & Liu, F.-C. Neural development of the neuregulin receptor ErbB4 in the cerebral cortex and the hippocampus: preferential expression by interneurons tangentially migrating from the ganglionic eminences. *Cereb. Cortex* **13**, 252–264 (2003).
19. Silberberg, G., Darvasi, A., Pinkas-Kramarski, R. & Navon, R. The involvement of ErbB4 with schizophrenia: association and expression studies. *Am. J. Med. Genet. B Neuropsychiatr. Genet.* **141B**, 142–148 (2006).
20. Woo, R.-S., Lee, J.-H., Yu, H.-N., Song, D.-Y. & Baik, T.-K. Expression of ErbB4 in the neurons of Alzheimer's disease brain and APP/PS1 mice, a model of Alzheimer's disease. *Anat. Cell Biol.* **44**, 116–127 (2011).
21. Nahar, L., Delacroix, B. M. & Nam, H. W. The role of parvalbumin interneurons in neurotransmitter balance and neurological disease. *Front. Psychiatry* **12**, 679960 (2021).
22. Bygrave, A. M. *et al.* Btbd11 supports cell-type-specific synaptic function. *Cell Rep.* **42**, 112591 (2023).
23. Lee, D. D. & Sebastian Seung, H. Algorithms for non-negative matrix factorization. *Advances in Neural Information Processing Systems* https://papers.nips.cc/paper/1861-algorithms-for-non-negative-matrix-factorization (2000).

24. Brunet, J.-P., Tamayo, P., Golub, T. R. & Mesirov, J. P. Metagenes and molecular pattern discovery using matrix factorization. *Proc. Natl. Acad. Sci. U. S. A.* **101**, 4164–4169 (2004).

25. Dickson, D. W. Apoptotic mechanisms in Alzheimer neurofibrillary degeneration: cause or effect? *J. Clin. Invest.* **114**, 23–27 (2004).

26. Goel, P. *et al.* Neuronal cell death mechanisms in Alzheimer's disease: An insight. *Front. Mol. Neurosci.* **15**, 937133 (2022).

27. Zeng, H. et al. Integrative in situ mapping of single-cell transcriptional states and tissue histopathology in a mouse model of Alzheimer's disease. Nat. Neurosci. 26, 430–446 (2023).

28. Dataset: 10x Genomics, Xenium In Situ Analysis of Alzheimer's Disease Mouse Model Brain Coronal Sections from One Hemisphere Over a Time Course, *In Situ Gene Expression dataset analyzed using Xenium Onboard Analysis 1.4.0,* (2023). Available from: https://www.10xgenomics.com/datasets/xenium-in-situ-analysis-of-alzheimers-disease-mouse-model-brain-coronal-sections-from-one-hemisphere-over-a-time-course-1-standard

29. Dataset: Allen Institute for Brain Science, University of Washington Alzheimer's Disease Research Center, and Kaiser Permanente Washington Health Research Institute (2022). Seattle Alzheimer's Disease Brain Cell Atlas (SEA-AD) -- 10x single nucleus RNAseq [Dataset]. AD Knowledge Portal. Available from: https://adknowledgeportal.synapse.org/Explore/Studies/DetailsPage/StudyDetails?Study=syn26223298

30. Hawrylycz, M. et al. SEA-AD is a multimodal cellular atlas and resource for Alzheimer's disease. Nat Aging. Oct;4(10):1331-1334. (2024)

31. Love, M. I., Huber, W. & Anders, S. Moderated estimation of fold change and dispersion for RNA-seq data with DESeq2. *Genome Biol.* **15**, 550 (2014).

32. Wickham, H. *Ggplot2: Elegant Graphics for Data Analysis*. (Springer, New York, NY, 2009).

33. Millard, S. P. *EnvStats: An R Package for Environmental Statistics*. (Springer, New York, NY, 2013).

34. Gaujoux, R. & Seoighe, C. A flexible R package for nonnegative matrix factorization. *BMC Bioinformatics* **11**, 367 (2010).

35. Csárdi, G. & Nepusz, T. The igraph software package for complex network research. *InterJournal* **Complex Systems**, 1695 (2006).

36. Tsukahara, T. *et al.* A transcriptional rheostat couples past activity to future sensory responses. *Cell* **184**, 6326–6343.e32 (2021).

37. Reimand, J., Kull, M., Peterson, H., Hansen, J. & Vilo, J. g:Profiler--a web-based toolset for functional profiling of gene lists from large-scale experiments. *Nucleic Acids Res.* **35**, W193–200 (2007).

38. Amezquita, R. A. *et al.* Orchestrating single-cell analysis with Bioconductor. *Nat. Methods* **17**, 137–145 (2020).

39. Lin, Y. *et al.* scMerge leverages factor analysis, stable expression, and pseudoreplication to merge multiple single-cell RNA-seq datasets. *Proc. Natl. Acad. Sci. U. S. A.* **116**, 9775–9784 (2019).

40. Geeleher, P., Gamazon, E. R., Seoighe, C., Cox, N. J. & Huang, R. S. Consistency in large pharmacogenomic studies. *Nature* **540**, E1–E2 (2016).

41. Danaher, P. *et al.* Insitutype: likelihood-based cell typing for single cell spatial transcriptomics. *bioRxiv* 2022.10.19.512902 (2022) doi:10.1101/2022.10.19.512902.

42. Sanz-Morello, B. *et al.* Complex IV subunit isoform COX6A2 protects fast-spiking interneurons from oxidative stress and supports their function. *EMBO J.* **39**, e105759 (2020).

43. Hinckelmann, M.-V. *et al.* Self-propelling vesicles define glycolysis as the minimal energy machinery for neuronal transport. *Nat. Commun.* **7**, 13233 (2016).

44. Yao, S. *et al.* Astrocytic lactate dehydrogenase A regulates neuronal excitability and depressive-like behaviors through lactate homeostasis in mice. *Nat. Commun.* **14**, 729 (2023).

45. Kokotos, A. C. *et al.* Phosphoglycerate kinase is a central leverage point in Parkinson's disease-driven neuronal metabolic deficits. *Sci. Adv.* **10**, eadn6016 (2024).

46. Vuletic, S. *et al.* Reduced CSF PLTP activity in Alzheimer's disease and other neurologic diseases; PLTP induces ApoE secretion in primary human astrocytes in vitro. *J. Neurosci. Res.* **80**, 406–413 (2005).

47. Xiyang, Y.-B. *et al.* COX5A plays a vital role in memory impairment associated with brain aging via the BDNF/ERK1/2 signaling pathway. *Front. Aging Neurosci.* **12**, 215 (2020).

48. Letts, J. A., Fiedorczuk, K. & Sazanov, L. A. The architecture of respiratory supercomplexes. *Nature* **537**, 644–648 (2016).

49. Tong, W.-H. & Rouault, T. A. Functions of mitochondrial ISCU and cytosolic ISCU in mammalian iron-sulfur cluster biogenesis and iron homeostasis. *Cell Metab.* **3**, 199–210 (2006).

50. Bischop, D. P., Orduz, D., Lambot, L., Schiffmann, S. N. & Gall, D. Control of neuronal excitability by calcium binding proteins: a new mathematical model for striatal fast-spiking interneurons. *Front. Mol. Neurosci.* **5**, 78 (2012).

51. Pelkey, K. A. *et al.* Hippocampal GABAergic inhibitory interneurons. *Physiol. Rev.* **97**, 1619–1747 (2017).

52. Meng, J. H. *et al.* In search of transcriptomic correlates of neuronal firing-rate adaptation across subtypes, regions and species: A Patch-seq analysis. *bioRxivorg* (2024) doi:10.1101/2024.12.05.627057.

53. Wengert, E. R. *et al.* Impaired excitability of fast-spiking neurons in a novel mouse model of KCNC1 epileptic encephalopathy. *bioRxivorg* (2024) doi:10.1101/2024.09.27.615463.

54. Uchida, T., Furukawa, T., Iwata, S., Yanagawa, Y. & Fukuda, A. Selective loss of parvalbumin-

positive GABAergic interneurons in the cerebral cortex of maternally stressed Gad1-heterozygous mouse offspring. *Transl. Psychiatry* **4**, e371 (2014).

55. Lazarus, M. S., Krishnan, K. & Huang, Z. J. GAD67 deficiency in parvalbumin interneurons produces deficits in inhibitory transmission and network disinhibition in mouse prefrontal cortex. *Cereb. Cortex* **25**, 1290–1296 (2015).
56. Eiraku, M. *et al.* DNER acts as a neuron-specific Notch ligand during Bergmann glial development. *Nat. Neurosci.* **8**, 873–880 (2005).
57. Sanchez-Mejias, E. *et al.* Distinct disease-sensitive GABAergic neurons in the perirhinal cortex of Alzheimer's mice and patients. *Brain Pathol.* **30**, 345–363 (2020).
58. Xu, Y., Zhao, M., Han, Y. & Zhang, H. GABAergic inhibitory interneuron deficits in Alzheimer's disease: Implications for treatment. *Front. Neurosci.* **14**, 660 (2020).
59. Zheng, X., Thompson, P. C., White, C. M. & Jin, X. Massively parallel in vivo Perturb-seq screening. *Nat. Protoc.* **20**, 1733–1767 (2025).
60. Adamovich, T., Zakharov, I., Tabueva, A. & Malykh, S. The thresholding problem and variability in the EEG graph network parameters. *Sci. Rep.* **12**, 18659 (2022).
61. Chen, W.-T. *et al.* Spatial transcriptomics and in situ sequencing to study Alzheimer's disease. *Cell* **182**, 976–991.e19 (2020).
62. Makaroff, C. A. & Zalkin, H. Regulation of Escherichia coli purF. Analysis of the control region of a pur regulon gene. *J. Biol. Chem.* **260**, 10378–10387 (1985).
63. Grubman, A. et al. A single-cell atlas of entorhinal cortex from individuals with Alzheimer's disease reveals cell-type-specific gene expression regulation. Nat. Neurosci. 22, 2087–2097 (2019).
64. Leng, K. et al. Molecular characterization of selectively vulnerable neurons in Alzheimer's disease. Nat. Neurosci. 24, 276–287 (2021).

65. Chen, S. et al. Spatially resolved transcriptomics reveals genes associated with the vulnerability of middle temporal gyrus in Alzheimer's disease. Acta Neuropathol. Commun. 10, 188 (2022).

66. Miyoshi, E. et al. Spatial and single-nucleus transcriptomic analysis of genetic and sporadic forms of Alzheimer's Disease. bioRxivorg (2023) doi:10.1101/2023.07.24.550282.

67. Gaur, P. et al. Single-nucleus and spatial transcriptomic profiling of human temporal cortex and white matter reveals key associations with AD pathology. Nat. Commun. 16, 10395 (2025).

68. Harris, K. D. et al. Classes and continua of hippocampal CA1 inhibitory neurons revealed by single-cell transcriptomics. PLoS Biol. 16, e2006387 (2018).

Acknowledgments

The authors would like to acknowledge Luiz G.N. de Almeida for assistance with analysis of public datasets.

Funding

Funding for this study was provided by a Canadian Institutes of Health Research Project Grant (#190215) to J.R.E.

Author contributions

D.J.T., B.A., Y.R., H.S and J.R.E. designed the research. H.S. and D.J.T. conducted the analyses and visualized the results. B.A., S.L., and K.R.G. performed the spatial transcriptomics experiments. D.J.T. and Y.R. performed the validation experiments. H.S., D.J.T., B.A., and J.R.E. interpreted the results. H.S. and D.J.T. and J.R.E wrote the manuscript. D.J.T., and J.R.E. critically revised the manuscript.

Competing Interests

The authors declare no competing interests.

Figure Legends

Fig. 1 | Nanostring GeoMx DSP data preprocessing and quality assessment. a An Illustrative representation of the mouse brain highlighting the retrosplenial cortex (RSC). b The specimen and slide configurations that show the groups and the number of specimens analyzed using two spatial transcriptomics platforms (GeoMX DSP N=3 WT, N=4 5xFAD; Xenium N=3 WT, N=3 5xFAD). c The tissue images from the GeoMx DSP with four fluorescent markers: SYTO13 (blue) for staining nucleic acid, PV (purple) for labelling interneurons, NeuN (green) for neurons, and Amyloid (red) for amyloid plaques. A specific region of interest (ROI) within the RSC is selected for the TG1F specimen, showcasing snapshots from four distinct segments: Interneuron (PV), Neuron (NeuN), Amyloid, and TN (triple-negative). d A flowchart summarizing the preprocessing steps including the reduction of probes/genes and AOIs (area-of-illuminations) remaining at each step and the normalization method applied to generate an analysis-ready profile from the GeoMx DSP data. A diamond symbol represents a filtering process, illustrating the number of Areas of Interest (AOIs) excluded at each step, based on the established threshold values. e Scatter plot that illustrates a positive correlation between the area size of AOIs and the corresponding number of nuclei, plotted along the X- and Y-axes, respectively. f (left) Violin plot depicts the distributions of the LOQ (limit of quantification) values across different segments; (right) Scatter pie chart shows the proportion of included (coloured) and excluded (grey) genes expressed below the LOQ values with axes representing mean expression and LOQ on a logarithmic scale. Box plots show the median (centre line), interquartile range (IQR; box bounds from 25th to 75th percentile), and whiskers extending to 1.5 × IQR from the box hinges; data points beyond the whiskers are plotted individually as outliers. g Bar plots elucidate the gene detection rate where the height of each bar signifies the number of AOIs within each segment. h Scatter plots show the results of principal component analysis annotated with different colour sets to represent each category with the analysis-ready profile. i Volcano plot identifies the differentially expressed genes between the PV and NeuN segments where red and blue dots indicate genes that are up- and down-regulated in PV relative to NeuN, respectively, using a Welch's t-test, two-sided. Source data are provided as a Source Data file. *Created in BioRender. Epp, J. (2026) https://BioRender.com/d2ajsun*

Fig. 2 | Correlation network construction and biological module identification. a A schematic workflow shows the step-by-step procedures for creating the correlation network from the outputs of non-negative matrix factorization (NMF). The subsequent step involves the utilization of a community detection algorithm which facilitates the identification of biological modules or a group of metagenes. These modules are distinguished based on their predominant presence in NMF outputs across various ranks and enable to selection of the best rank for downstream analysis. Once the rank is set, the relationship between metagenes and specimens is established. b Venn diagram displays the intersection of MAGs (metagene-associated genes) with a representation of five distinct genes from each category. c Bar graph displays the significant enrichment of GO (Gene Ontology) terms within each MAG category based on the hypergeometric distribution. The height of each bar is indicative of the significance level associated with each GO term. GO term enrichment was assessed using the hypergeometric test (one-sided, right-tailed) via g:Profiler, with multiple comparisons corrected using the g:SCS method (significance threshold: adjusted $P < 0.05$). d Correlation networks highlight the specimen

representations where nodes are displayed to represent specimens that exhibit the highest coefficient values. Additionally, community annotations that are marked with a number sign are annotated and defined according to the community search methodology outlined previously. e Circular bar plots illustrate the coefficient values distribution across metagenes within a specimen. The height of each bar corresponds to the geometric mean of the coefficient values for each sample, offering an understanding of variability. Source data are provided as a Source Data file.

Fig. 3 | Xenium data for RSC and differential expression analysis. a Tissue snapshots highlight the regions of interest (ROI) in the retrosplenial cortex (RSC) across specimens. The visualization employed a colour-coding scheme based on k-means clustering from Xenium Ranger by default to delineate cellular distributions effectively. b Density ridgeline plot elucidate the distributions of the number of Tx per cell across specimens. c (left) Scatter plot exhibits the correlation coefficient values between consecutive specimens; the expression accumulation of the PV segment from GeoMx DSP and that of RSC cells on the X-axis and between NeuN segment and RSC cells on the Y-axis using the Spearman correlation. (right) Bar plot depicts the distribution of correlation across specimens with a particular emphasis on 16 genes where the Spearman rho exceeded 0.9. d Volcano plot identifies the differentially expressed genes between the TG and WT groups where red and blue dots indicate genes that are up- and down-regulated in TG relative to WT, respectively, using the Wilcoxon rank sum test, two-sided. e t-SNE (t-distributed Stochastic Neighbor Embedding) plots to categorize two distinct annotations: (left) specimen annotation and (right) k-means clustering results annotation where k is set to seven. f Violin plots display the expression levels of specific genes within each identified cluster for a detailed view of gene expression patterns across clusters. Box plots show the median (centre line), interquartile range (IQR; box bounds from 25th to 75th percentile), and whiskers extending to 1.5 × IQR from the box hinges; data points beyond the whiskers are plotted individually as outliers. g Cell-type map snapshots using the k-means clustering showcase cell distribution in TG and WT specimens. Specific clusters, such as Cluster 1 (green), were highlighted for detailed examination including the Tx locations within each tissue sample along with the zoomed-in snapshots with a dotted line. h Pie charts represent the cellular composition within each cluster to quantitatively summarize the distribution of cell types. Source data are provided as a Source Data file.

Fig. 4 | Integrative analysis of the spatial transcriptomics data from two distinct platforms. a (top) An illustration displays two input matrices to infer cell type. The Venn diagram depicts the intersection of genes between the NMF (non-negative matrix factorization) features within each segment and the genes listed in the Xenium panel. (bottom) Stacked barplot displays the proportions of cell types inferred using the NMF outputs as a cell-type reference. b Tissue snapshots using the Xenium Explorer reveal cell types; (left) cell types inferred as PV and NeuN are highlighted in purple and green. (centre) Each cell type in PV is marked in three different colours (red, blue, and purple), whereas NeuN cells are represented in a grey hue. (right) Zoomed-in views with the Tx maintaining the same regions and resolution as shown in Fig. 3g. c Volcano plot identifies differentially expressed genes between M1PV cells and other cell populations where red and blue dots indicate genes that are up- and down-regulated in M1PV cells relative to the rest of the cells. Differential expression was assessed using the Wilcoxon rank-sum test (two-sided), as implemented in the presto R package, with p-values adjusted for multiple

comparisons using the Benjamini-Hochberg (BH) method (significance thresholds: adjusted $P < 0.05$, $|\log2 \text{ fold-change}| > 0.5$). d Four additional brain sections are selected to validate the findings in this study, namely SUB (subiculum), VIS (visual cortex), ENT (entorhinal cortex), and CA1 region of the hippocampus, to compare the level of Tx across sections. e t-SNE (t-distributed Stochastic Neighbor Embedding) plots to categorize two distinct annotations: (left) specimen annotation and (right) five different brain sections. f Differential expression analysis results across sections show on a Scatter plot where the X- and Y-axes represent genes and the log2 fold-change, respectively, Significance is denoted by letters representing each brain region with colours indicating an adjusted P-value of less than 0.05 using the Wilcoxon rank sum test, two-sided, otherwise non-significant results are indicated by letters that are greyed out. Source data are provided as a Source Data file.

Fig. 5 | Validation of down-regulated genes in transgenic mice identified by dual spatial transcriptomic platforms. a Schematic workflow outlining the stepwise gene selection process, including the number of genes retained at each stage and the inclusion or exclusion of established genes for subsequent validation. **b** Representative RNAscope images showing signal intensity for each gene. PV+ cells have been delineated for visualization. Scale bars represent 20 μm. **c** Bar plots of mean RNA labelling intensity from RNAscope for each group: wild-type (WT, blue) and transgenic (TG, red). Data shown is mean +/- SEM and each dot indicates one mouse (n=5 5xFAD, n=4 WT). Data were analyzed using unpaired two-tailed t-tests. *Pvalb:* $t(7)=3.7$, $p = 0.0075$, *Gad1:* $t(7)=2.58$, $p=0.037$, *Dner:* $t(7)=2.81$, $p=0.026$, *Cox6a2:* $t(7)=4.32$, $p=0.0035$. **d** Representative immunohistochemistry (IHC) images showing signal intensity for each protein of interest. PV+ cells have been delineated for visualization. Scale bars represent 20 μm. **e** Bar plots showing protein intensity quantified from IHC for WT and TG groups, with the same colour scheme as in (c). Data shown is mean +/- SEM and each dot indicates one mouse (n=5 5xFAD, n=5 WT). Pvalb*:* $t(8)=4.5$, $p = 0.002$, Gad1*:* $t(8)=3.14$, $p=0.014$, Dner*:* $t(8)=3.77$, $p=0.0055$, Cox6a2*:* $t(8)=2.77$, $p=0.024$ Source data are provided as a Source Data file.

Fig. 6 | Proposed mechanistic pathway of PV+ interneuron vulnerability in Alzheimer's Disease. a The down-regulation of *Cox6a2* in PV+ interneurons of TG mice impairs mitochondrial function by reducing complex IV activity and ATP production. **b** With down-regulated *Pvalb* expression, PV+ interneurons of TG mice have compromised calcium buffering capacity which can lead to increased cytosolic calcium and impair the precision of fast-spiking firing patterns. **c** *Gad1* expression is critical in the synthesis of GABA, therefore, its down-regulation in TG mice can impair the ability of PV+ interneurons to perform adequate synaptic inhibition. **d** Along with impaired synaptic function, the down-regulation of *Dner* in TG mice impairs notch signalling. These impairments have consequences on dendritic arborization and synapse density. *Created in BioRender. Epp, J. (2026) https://BioRender.com/ajn3252*

Editorial Summary
Combining two spatial transcriptomics platforms in female Alzheimer's model mice, the authors identify parvalbumin interneurons in the retrosplenial cortex that are selectively vulnerable to disease, revealing gene markers of early neuronal damage.

Peer review information: *Nature Communications* thanks Sara Calafate and the other, anonymous, reviewers for their contribution to the peer review of this work. A peer review file is available.

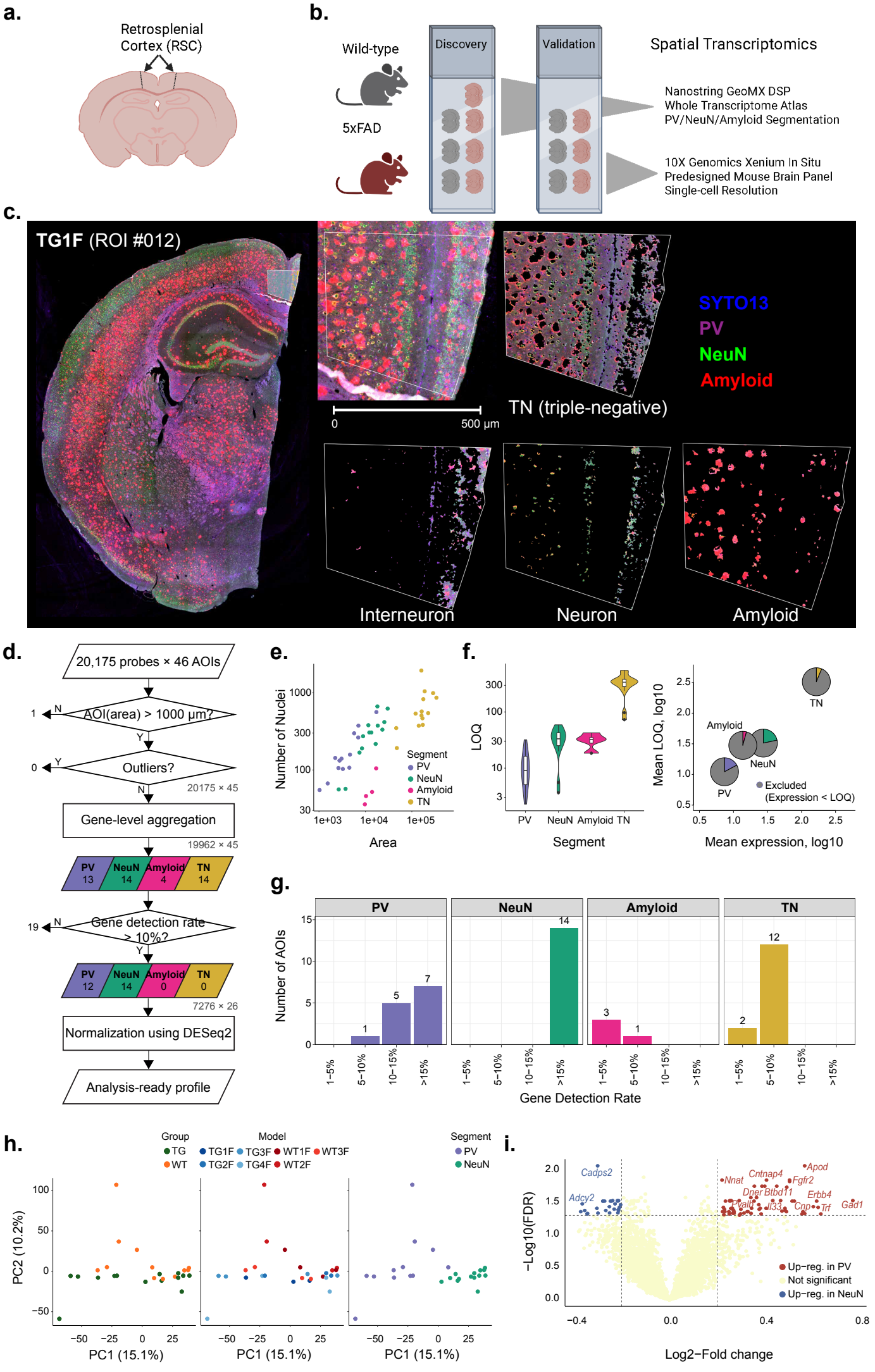
a.
Retrosplenial
Cortex (RSC)
b.
Wild-type
5xFAD
Discovery
Validation
Spatial Transcriptomics
Nanostring GeoMX DSP
Whole Transcriptome Atlas
PV/NeuN/Amyloid Segmentation
10X Genomics Xenium In Situ
Predesigned Mouse Brain Panel
Single-cell Resolution
c.
TG1F (ROI #012)
SYTO13
PV
NeuN
Amyloid
0
500 µm
TN (triple-negative)
Interneuron
Neuron
Amyloid
d.
20,175 probes × 46 AOIs
AOI(area) > 1000 µm?
Outliers?
20175 × 45
Gene-level aggregation
19962 × 45
PV 13
NeuN 14
Amyloid 4
TN 14
Gene detection rate > 10%?
PV 12
NeuN 14
Amyloid 0
TN 0
7276 × 26
Normalization using DESeq2
Analysis-ready profile
e.
Number of Nuclei
Area
Segment
PV
NeuN
Amyloid
TN
f.
LOQ
Segment
Mean LOQ, log10
Mean expression, log10
Excluded
(Expression < LOQ)
g.
PV
NeuN
Amyloid
TN
Number of AOIs
Gene Detection Rate
1–5%
5–10%
10–15%
>15%
h.
Group
TG
WT
TG1F
TG2F
TG3F
TG4F
WT1F
WT2F
WT3F
WT2F
Model
Segment
PV
NeuN
PC2 (10.2%)
PC1 (15.1%)
i.
−Log10(FDR)
Log2−Fold change
Cadps2
Adcy2
Nnat
Cntnap4
Apod
Fgfr2
Dner
Btbd11
Erbb4
Cnp
Trf
Gad1
Up−reg. in PV
Not significant
Up−reg. in NeuN

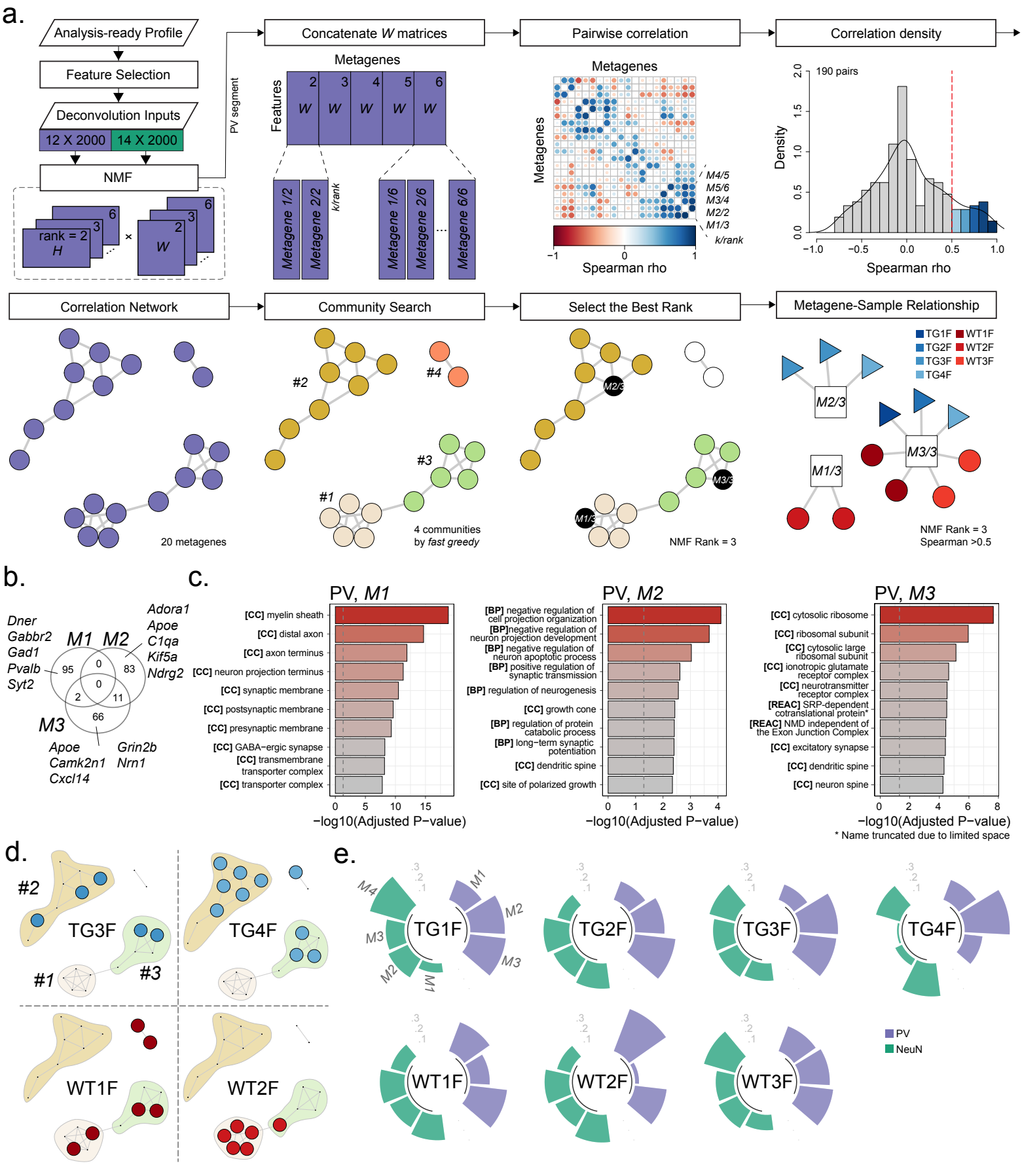
a.
Analysis-ready Profile
Feature Selection
Deconvolution Inputs
12 X 2000
14 X 2000
NMF
PV segment
rank = 2
H
W
Concatenate W matrices
Metagenes
Features
Metagene 1/2
Metagene 2/2
Metagene 1/6
Metagene 2/6
Metagene 6/6
k/rank
Pairwise correlation
Metagenes
M4/5
M5/6
M3/4
M2/2
M1/3
Spearman rho
Correlation density
190 pairs
Density
Spearman rho
Correlation Network
20 metagenes
Community Search
4 communities
by fast greedy
Select the Best Rank
NMF Rank = 3
Metagene-Sample Relationship
TG1F
TG2F
TG3F
TG4F
WT1F
WT2F
WT3F
M2/3
M3/3
M1/3
NMF Rank = 3
Spearman >0.5
b.
Dner
Gabbr2
Gad1
Pvalb
Syt2
M1
M2
Adora1
Apoe
C1qa
Kif5a
Ndrg2
M3
Apoe
Camk2n1
Cxcl14
Grin2b
Nrn1
c.
PV, M1
[CC] myelin sheath
[CC] distal axon
[CC] axon terminus
[CC] neuron projection terminus
[CC] synaptic membrane
[CC] postsynaptic membrane
[CC] presynaptic membrane
[CC] GABA−ergic synapse
[CC] transmembrane transporter complex
[CC] transporter complex
−log10(Adjusted P−value)
PV, M2
[BP] negative regulation of cell projection organization
[BP] negative regulation of neuron projection development
[BP] negative regulation of neuron apoptotic process
[BP] positive regulation of synaptic transmission
[BP] regulation of neurogenesis
[CC] growth cone
[BP] regulation of protein catabolic process
[BP] long−term synaptic potentiation
[CC] dendritic spine
[CC] site of polarized growth
−log10(Adjusted P−value)
PV, M3
[CC] cytosolic ribosome
[CC] ribosomal subunit
[CC] cytosolic large ribosomal subunit
[CC] ionotropic glutamate receptor complex
[CC] neurotransmitter receptor complex
[REAC] SRP-dependent cotranslational protein*
[REAC] NMD independent of the Exon Junction Complex
[CC] excitatory synapse
[CC] dendritic spine
[CC] neuron spine
−log10(Adjusted P−value)
* Name truncated due to limited space
d.
#2
TG3F
#1
#3
TG4F
WT1F
WT2F
e.
M4
M1
M2
M3
TG1F
TG2F
TG3F
TG4F
WT1F
WT2F
WT3F
PV
NeuN

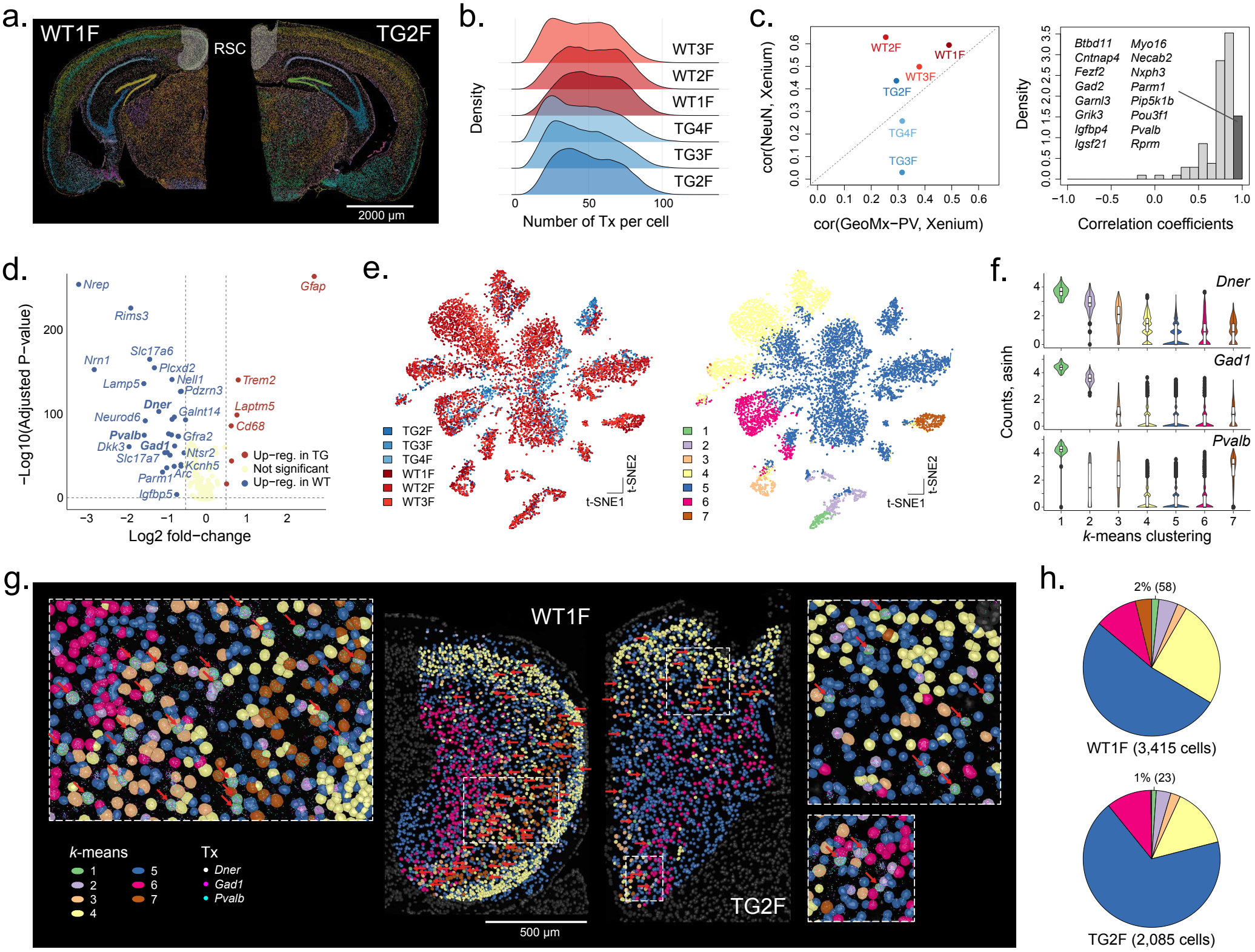
a.
WT1F
RSC
TG2F
2000 µm
b.
WT3F
WT2F
WT1F
TG4F
TG3F
TG2F
Density
0
50
100
Number of Tx per cell
c.
WT2F
WT1F
WT3F
TG2F
TG4F
TG3F
cor(NeuN, Xenium)
cor(GeoMx−PV, Xenium)
Btbd11
Cntnap4
Fezf2
Gad2
Garnl3
Grik3
Igfbp4
Igsf21
Myo16
Necab2
Nxph3
Parm1
Pip5k1b
Pou3f1
Pvalb
Rprm
Density
Correlation coefficients
d.
Nrep
Rims3
Slc17a6
Nrn1
Plcxd2
Nell1
Lamp5
Pdzrn3
Dner
Galnt14
Neurod6
Pvalb
Gfra2
Dkk3
Gad1
Slc17a7
Ntsr2
Kcnh5
Parm1
Arc
Igfbp5
Gfap
Trem2
Laptm5
Cd68
Up−reg. in TG
Not significant
Up−reg. in WT
−Log10(Adjusted P−value)
Log2 fold−change
e.
TG2F
TG3F
TG4F
WT1F
WT2F
WT3F
t-SNE1
t-SNE2
1
2
3
4
5
6
7
f.
Dner
Gad1
Pvalb
Counts, asinh
k-means clustering
g.
WT1F
TG2F
500 µm
k-means
Tx
Dner
Gad1
Pvalb
h.
2% (58)
WT1F (3,415 cells)
1% (23)
TG2F (2,085 cells)

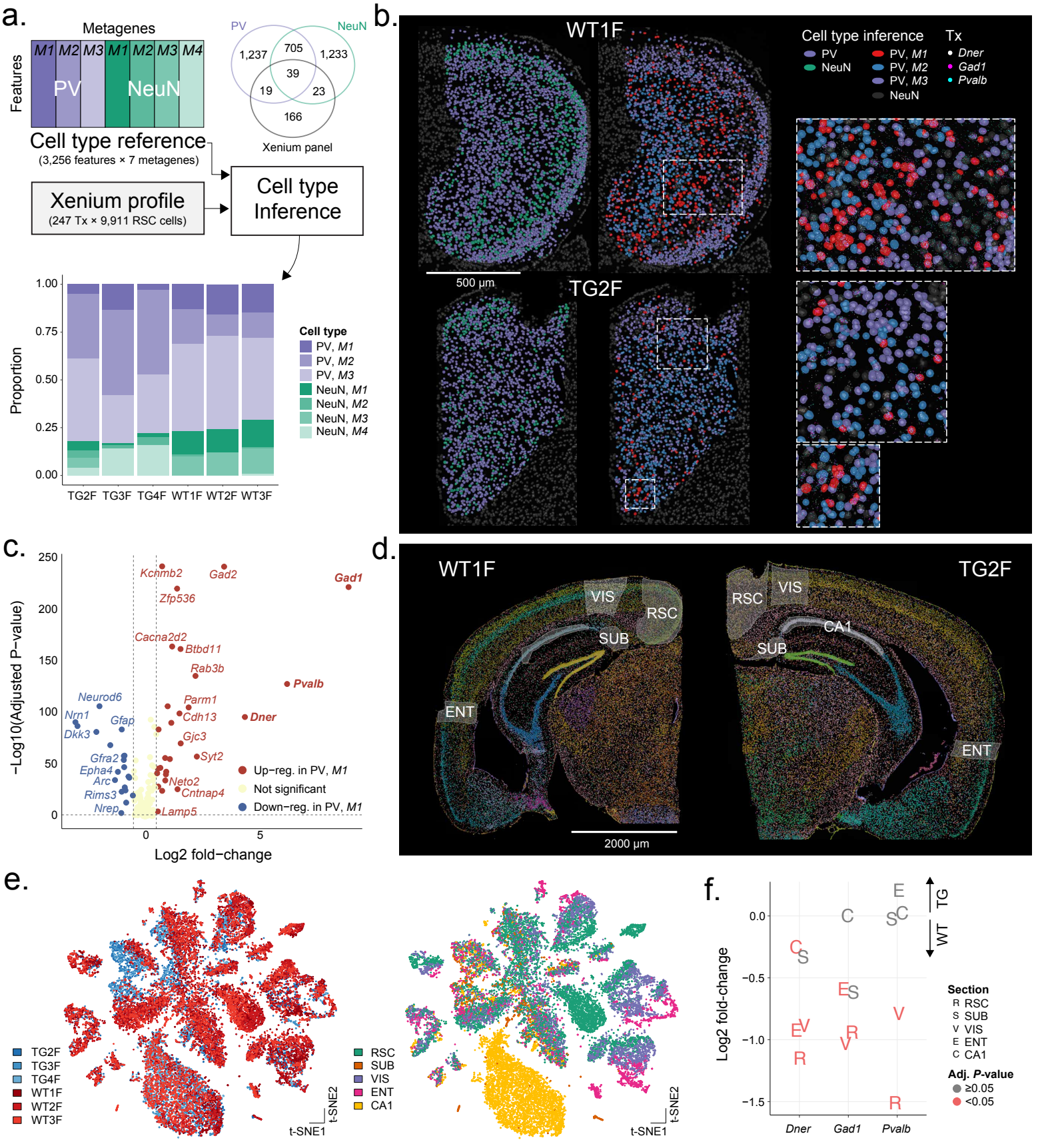
a.
Metagenes
Features
M1 M2 M3 M1 M2 M3 M4
PV
NeuN
PV
NeuN
1,237
705
1,233
39
19
23
166
Xenium panel
Cell type reference
(3,256 features × 7 metagenes)
Xenium profile
(247 Tx × 9,911 RSC cells)
Cell type Inference
Proportion
1.00
0.75
0.50
0.25
0.00
TG2F TG3F TG4F WT1F WT2F WT3F
Cell type
PV, M1
PV, M2
PV, M3
NeuN, M1
NeuN, M2
NeuN, M3
NeuN, M4
b.
WT1F
TG2F
500 µm
Cell type inference
PV
NeuN
PV, M1
PV, M2
PV, M3
NeuN
Tx
Dner
Gad1
Pvalb
c.
−Log10(Adjusted P−value)
Log2 fold−change
Kcnmb2
Gad2
Gad1
Zfp536
Cacna2d2
Btbd11
Rab3b
Pvalb
Neurod6
Parm1
Nrn1
Gfap
Cdh13
Dner
Dkk3
Gjc3
Gfra2
Syt2
Epha4
Arc
Neto2
Rims3
Cntnap4
Nrep
Lamp5
Up−reg. in PV, M1
Not significant
Down−reg. in PV, M1
d.
WT1F
TG2F
VIS
RSC
SUB
ENT
CA1
2000 µm
e.
TG2F
TG3F
TG4F
WT1F
WT2F
WT3F
RSC
SUB
VIS
ENT
CA1
t-SNE1
t-SNE2
f.
Log2 fold-change
0.0
−0.5
−1.0
−1.5
Dner
Gad1
Pvalb
TG
WT
Section
R RSC
S SUB
V VIS
E ENT
C CA1
Adj. P-value
≥0.05
<0.05

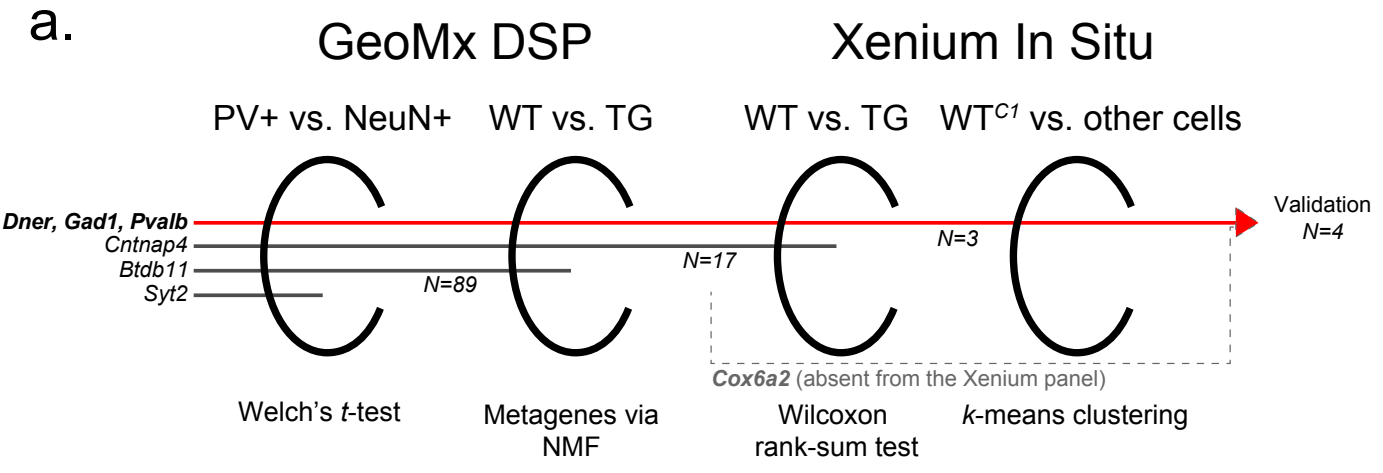
a.
GeoMx DSP
Xenium In Situ
PV+ vs. NeuN+
WT vs. TG
WT vs. TG
WT^C1 vs. other cells
Dner, Gad1, Pvalb
Cntnap4
Btdb11
Syt2
N=89
N=17
N=3
Validation
N=4
Cox6a2 (absent from the Xenium panel)
Welch's t-test
Metagenes via NMF
Wilcoxon rank-sum test
k-means clustering

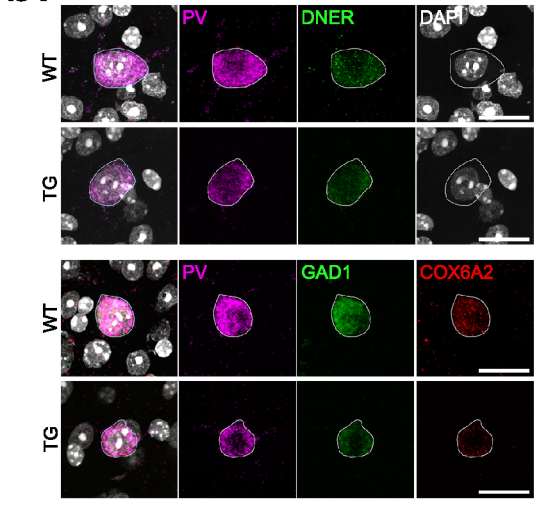
b.
WT
TG
PV
DNER
DAPI
GAD1
COX6A2

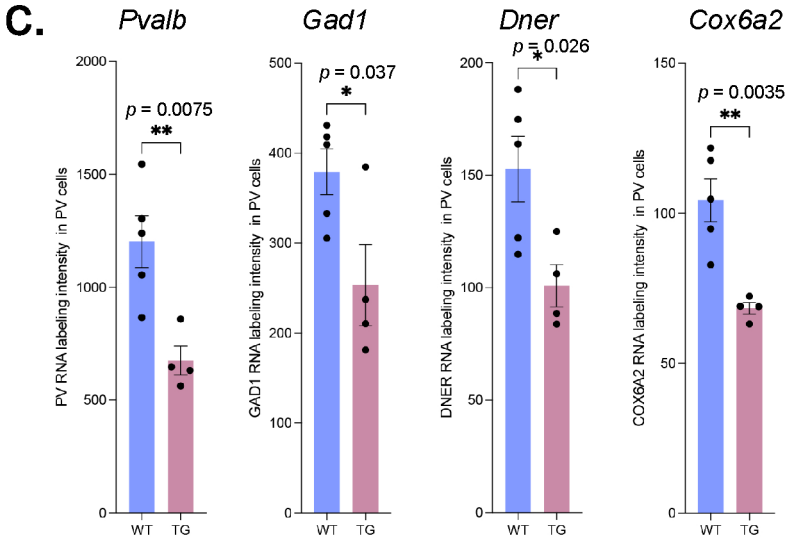
c.
Pvalb
Gad1
Dner
Cox6a2
p = 0.0075
p = 0.037
p = 0.026
p = 0.0035
PV RNA labeling intensity in PV cells
GAD1 RNA labeling intensity in PV cells
DNER RNA labeling intensity in PV cells
COX6A2 RNA labeling intensity in PV cells
WT
TG

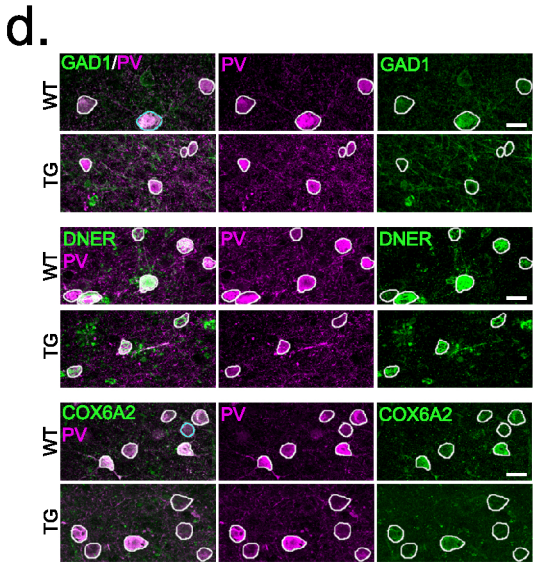
d.
WT
TG
GAD1/PV
PV
GAD1
DNER
COX6A2

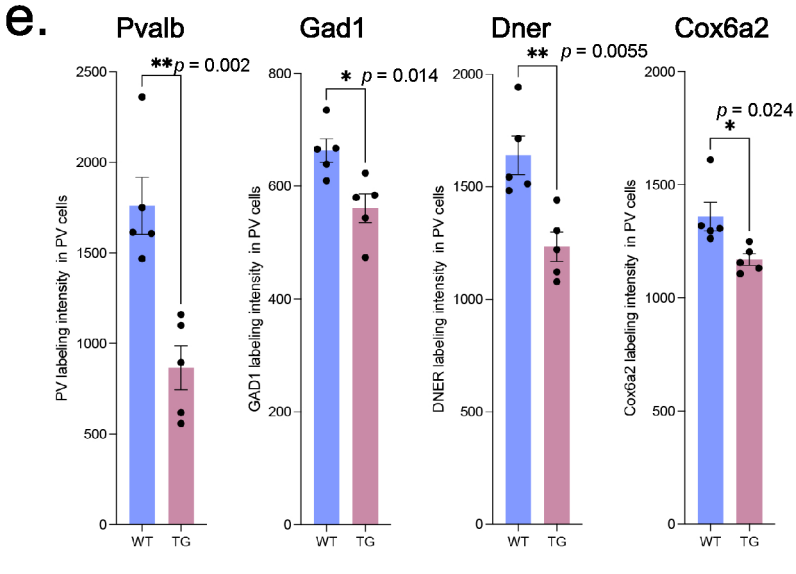
e.
Pvalb
Gad1
Dner
Cox6a2
p = 0.002
p = 0.014
p = 0.0055
p = 0.024
PV labeling intensity in PV cells
GAD1 labeling intensity in PV cells
DNER labeling intensity in PV cells
Cox6a2 labeling intensity in PV cells
WT
TG

a. Mitochondrial dysfunction

Cox6a2

ATP production

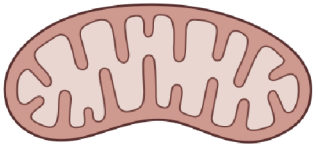

b. Loss of fast-spiking fidelity

Pvalb

Ca2+ buffering

Spike timing

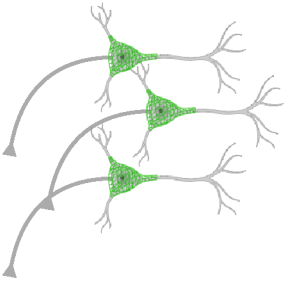

Increased PV+ interneuron vulnerability

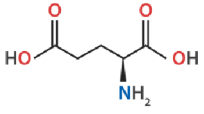

Gad1

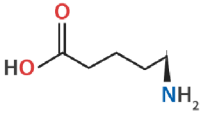

Glutamate

GABA

Gad1

GABA levels

Synaptic inhibition

c. Impaired synaptic inhibition

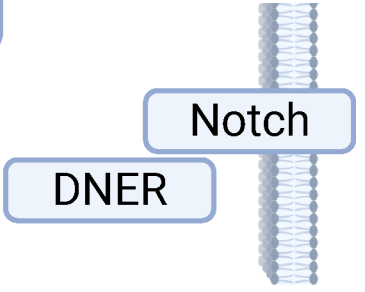

Dner

Dendritic arborization

Synaptic density

d. Dendritic and synaptic atrophy